

# Creation Mechanism of Devil's Staircase Surface and Unstable and Stable Periodic Orbit in the Anisotropic Kepler Problem

Tokuzo Shimada<sup>1</sup>, Keita Sumiya<sup>2</sup>, Kazuhiro Kubo<sup>3</sup>

<sup>1</sup>Department of physics, School of Science and Technology, Meiji University, Higashimita 1-1-1, Tama, Kawasaki, Kanagawa, 214-8571, Japan

<sup>2</sup>Faculty of Global Media Studies, Komazawa University, Komazawa 1-23-1, Setagaya, Tokyo, 154-0012, Japan

<sup>3</sup>Department of Physics, Bar-Ilan University, Ramat-Gan 52900, Israel

E-mail:

tshimada@gravity.mind.meiji.ac.jp, ksumiya@komazawa-u.ac.jp, kkubo3@gmail.com

## 1. Introduction

We study two dimensional AKP (1) which admits a binary coding of the orbit. We focus our attention on the coexistence of the unstable and stable POs of the same code. We clarify the mechanism of a salient bifurcation process where, under decreasing system anisotropy, an unstable PO ( $U$ ) bifurcates into a stable PO ( $S$ ) and a new type of unstable PO ( $U'$ ). Distinguishing self-retracing and non-self-retracing type of PO by ' $R$ ' and ' $NR$ ', the bifurcation is  $U(R) \rightarrow S(R) + U'(NR)$ .

Let us first have a quick look at AKP. It is a vital testing ground of quantum chaos ever since Gutzwiller cultivated it [1–7] to test his periodic orbit theory (POT) in its high anisotropy regime ( $\gamma \equiv \nu/\mu \leq 0.2$ ). Because of the Coulomb interaction, it is not a KAM system and reveals an abrupt transition from the integrable limit if  $\gamma$  is reduced from one [8]. The region ( $0.7 \leq \gamma \leq 0.85$ ) interestingly exhibits critical statistics, which is reminiscent of the Anderson localization in condensed matter physics [8–11]. Recently, we have successfully extracted information of 2-dim low-rank unstable POs (sequence, period and even the Lyapunov exponent) from quantized 3-dim AKP levels via inverse use of POT and suitable symmetrization [12]. We have also shown that the quantum scar in AKP is robust and survives under successive avoiding level crossings during large variation of the anisotropy [13]. It is worth to note that AKP can be realized by a semiconductor with donor impurity and experimental manufacturing has been advanced [14, 15].

Now, there is a long standing question regarding the PO in AKP. It was shown by Gutzwiller [2] and rigorously probed by Devaney [16] that, for an arbitrary given binary sequence (or code), there exists at least one initial point for a PO which evolves

realizing the sequence, provided that  $\gamma < 8/9$ <sup>1</sup>. Here the PO is isolated and unstable.

The *uniqueness* of a PO for a given code, on the other hand, was conjectured by Gutzwiller from extensive numerical investigation, while Broucke found two stable POs as a counter example [18] in the low anisotropy region<sup>2</sup>. An overview by 1990 is given in the Gutzwiller's book [19].

Recently, Contopoulos and Harsoula have found that there are many stable POs not necessarily in the low anisotropy regime. This implies that AKP is not an Anosov system [20]. Unfortunately, their PO search is limited to the case of perpendicular emission from the heavy axis, and hence is not capable of correctly detecting the  $U'(NR)$  in the case of the bifurcation  $U(R) \rightarrow S(R) + U'(NR)$ , since  $U'(NR)$  does not have any perpendicular crossing of the heavy axis.

This paper is organized as follows. In section 2, three basics points are established. (1) One-time map. A suitably compactified 2-dim rectangle  $D$  is chosen as an initial value domain of the AKP flow and we work out the one-time map  $\mathcal{F} : D_0 \rightarrow D_1$ . In fact, the map  $\mathcal{F}|_I$  restricted to the collision manifold  $I(\subset D)$  is investigated by Gutzwiller [2] and we integrate his wisdom into a convenient form. It is extended to the interior combining numerical analysis (figure 4 and 5).

(2) A level  $N$  devil's staircase surface (DSS) and associated tiling of  $D_0$  by the base *ribbons* of the steps.

(3) PO trapping. An initial point of a PO of a given code must lie in the cross-sectional area of a future (F) and a past (P) ribbon of the respective F and P code<sup>3</sup>.

Then, in section 3, how the level  $N + 1$  DSS is created from level  $N$  one is clarified. The mechanism gives, on one hand, a simple proof of the properness of the tiling (monotonicity of the surface)—traversing ribbons from left to right, the height of step always increases. On the other hand, it points out the possibility of a non-shrinking ribbon at large  $N$ .

In section 4, it is shown explicitly that there are two fates of ribbons at large  $N$  depending on the code and the anisotropy.

(A) In most cases, both the F and P ribbons shrink at large  $N$ . Then the trapped PO, in the cross-sectional area, is singled out at the crossing of F and P asymptotic curves.

(B) Below certain anisotropy, there emerges an exceptional ribbon, which stops shrinkage at finite  $N$ .<sup>4</sup> We show this occurs just when the future and past ribbons become

1 In [2], a candidate 'trajectory' for the code is constructed by combining arcs (each satisfies the equation of motion). Joining them into a smooth PO requires the existence of the maximum of joint virial function, which is shown to be probable. In [16], stable and unstable manifolds of distinct hyperbolic singularities of AKP Hamilton flow is shown to cross transversely along bi-collision orbits.

2 *Devaney instigated to find a counter example in the form of a stable PO* [19]. One is  $(+ - -)^2$  (rank 3 and exists for  $\gamma > 0.5723511979186147$ , and the other is  $(+ - + + -)^2$  (rank 5) and  $\gamma > 0.7216809344182386$ . The threshold values here are from our high precision measurement.

3 This is noted by Gutzwiller (p.169 in [7]). At the same place, the difficulty to use it to locate an unstable PO due to high Lyapunov exponent is mentioned (even for rank 5). Our approach using ribbons (rather than constructing unstable and stable manifold) can easily overcome it.

4 This is also noticed by Gutzwiller with respect to Broucke's island as *a short but non-vanishing interval* (of the 1-dim devil's staircase). (p.409 in [7]. Also see [5]). In terms of unstable manifold

tangent each other. Then, the initial points of unstable and stable PO are both contained in the cross-sectional area of non-shrinking future and past ribbons. The emergence of such non-shrinking ribbons in turn induces a salient code-preserving bifurcation:  $U(R) \rightarrow S(R) + U'(NR)$  within  $Y$  symmetric PO (figure 9–11). We explain this pattern by symmetry and topology consideration of PO (figure 14) and conjecture that it should occur for  $Y$ -symmetric, rank odd PO.

Section 5 is devoted to the application of the ribbon tiling to the PO search in AKP. In order to search PO of all possible symmetry types, brute force shooting would require the search in the vast two-dimensional free parameter space, which is not feasible for high rank PO. However, two-step search—firstly search the relevant ribbon and then the PO within it—clearly reduces the task to quasi-one-dimensional. Based on this idea, we devise a concrete algorithm of exhaustive search, which is sensitive to the coexistence of stable and unstable POs. We firstly take a high rank PO ( $n = 15$ ) as an example and show it does bifurcate as  $U(R) \rightarrow S(R) + U'(NR)$ . We pursue the final POs to the very low anisotropy region ( $\gamma > 8/9$ ), and find a second bifurcation  $S(R) \rightarrow S'(R) + S''(NR)$ . (See figure 16). We find these successive bifurcations are in accordance with the topology and symmetry classification. Then, we turn to an extensive PO search, rank extending to  $n = 10$ , and at high anisotropy  $\gamma = 0.2$ . This is important since a question is cast on the possible existence of a stable PO even at high anisotropy regime [20]. We find all the 19284 isolated unstable POs just predicted from symmetry analysis (with a correction for the new symmetric type ( $O$  type) PO at rank seven and nine). and nothing else. This confirms (within the set-up resolution) the uniqueness of a PO at a given code (modulo symmetry equivalence) at  $\gamma = 0.2$ . The above unstable POs are used to verify Gutzwiller's approximate action formula. Actions of 13648 POs at rank  $n = 10$  are predicted (with its only two parameters fixed by 44 POs at  $n = 5$ ) with amazing accuracy (MSD=0.0536). (See figure 23 and table 4).

## 2. Devil's Staircase Surface and the One-time Map

### 2.1. Gutzwiller's rectangle

The Hamiltonian of two-dimensional AKP is given by

$$H = \frac{u^2}{2\mu} + \frac{v^2}{2\nu} - \frac{1}{r}, \quad (r \equiv \sqrt{x^2 + y^2}, \mu > \nu) \quad (1)$$

where  $u \equiv p_x, v \equiv p_y$  and the mass anisotropy is proportional to  $1 - \gamma$  with  $\gamma \equiv \nu/\mu < 1$ . Because  $\ddot{y}/\ddot{x} = (\mu/\nu)y/x > y/x$ , the orbit tends to cross the heavy  $x$ -axis more frequently. Thus, the Poincaré surface of section (PSS) is specified by the condition  $y = 0$  in the phase space, and we can encode the orbit by the code of  $a_i = \pm 1$ , the sign of  $x_i$  at the  $i$ -th crossing of the orbit with the  $x$ -axis. The future code is analysis, the island opens after *some of its* (binary tree's) *branches have been bundled together*.

$(a_0, a_1, \dots)$  and the past is  $(a_0, a_{-1}, \dots)$ <sup>5</sup>. The constant energy condition determines the kinematically allowed region on the PSS (the physical region for short). As the potential is homogeneous in coordinates, the system has a scaling property. Any value for the energy is equivalent and we take  $H = -1/2$  by convention. Under  $y = 0$  and  $H = -1/2$ , the domain of initial coordinates in the PSS is

$$\mathfrak{D} = \left\{ (x, u) \mid |x| \leq \frac{2}{1 + u^2/\mu} \text{ and } -\infty \leq u \leq +\infty \right\}, \quad (2)$$

which is a ‘lips’-like region in figure 2.1(a)<sup>6</sup>.

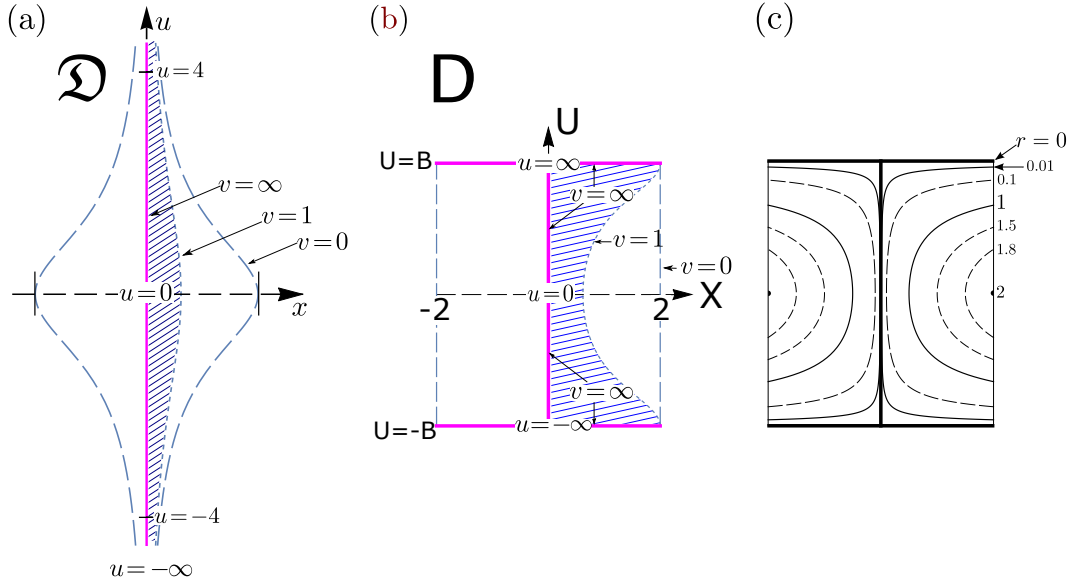


**Figure 1.** (a) The initial domain  $\mathfrak{D}$  on the Poincaré surface of section ( $y = 0$ ). (b) Gutzwiller rectangle  $D$ . I-shaped *backbone* (solid line) is the collision manifold ( $r = 0$ ). Graphs are drawn to scale (at  $\gamma = 0.2$ ,  $B = 2.349$ ). The map  $\mathfrak{D} \rightarrow D$  preserves area. For instance, hatched regions ( $-\infty < u < \infty$ ,  $1 \leq v$ ) in  $\mathfrak{D}$  and  $D$  have the same area. (c) Equi- $r$  contours in  $D$  approach the backbone at  $r \rightarrow 0$ .

The part of  $\mathfrak{D}$  where  $r = 0$  (the location of the collision) is the core line of  $\mathfrak{D}$  (the  $u$ -axis) where  $v = \infty$  and  $-\infty \leq u \leq \infty$ . Following Gutzwiller we compactify  $\mathfrak{D}$  by an area preserving map

$$X = x(1 + u^2/\mu), \quad U = \sqrt{\mu} \arctan(u/\sqrt{\mu}) \quad (3)$$

into a rectangle

$$D = \left\{ (X, U) \mid |X| \leq 2 \text{ and } |U| \leq B \equiv \frac{\sqrt{\mu}\pi}{2} \right\} \quad (4)$$

<sup>5</sup> To treat the future and past DSS on an equal footing we include  $a_0$  in both sequences. The choice of the present ( $i = 0$ ) is immaterial due to the time-translation invariance.

<sup>6</sup> In fact the physical region is a double-cover of figure 2.1(a) because  $v$  can be either positive or negative. Hereafter we limit our consideration to  $\mathfrak{D}$  with  $v \geq 0$ , since the case  $v < 0$  is obtained by a simple reflection with respect to the  $y$ -axis.

depicted in figure 2.1(b). The collision occurs on the I-shaped backbone of  $D$  :

$$I = \{ (X, U) \mid |X| \leq 2 \text{ and } U = \pm B \} \cup \{ (X, U) \mid X = 0 \text{ and } |U| \leq B \}. \quad (5)$$

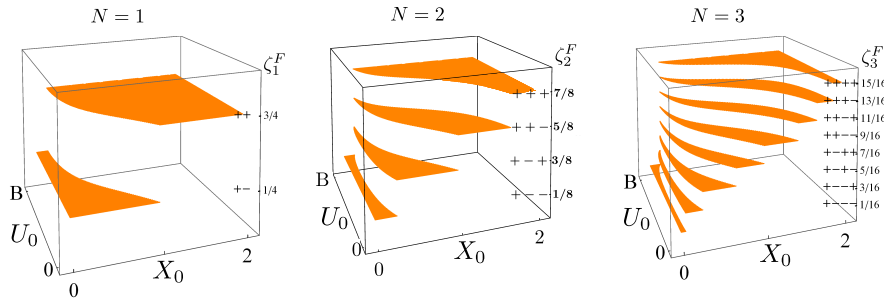
We call I collision manifold.

## 2.2. Symbolic coding of orbits and Devil's staircase surface

The future and past surfaces over  $D$  at level  $N$  are respectively described by the height functions

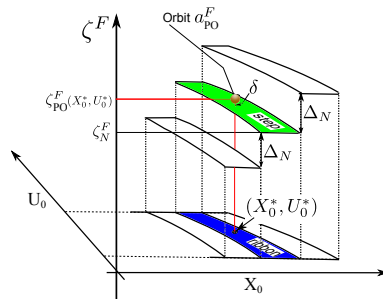
$$\zeta_N^F(X_0, U_0) \equiv \sum_{j=0}^N \frac{1}{2^{j+1}} a_j(X_0, U_0), \quad \zeta_N^P(X_0, U_0) \equiv \sum_{j=0}^N \frac{1}{2^{j+1}} a_{-j}(X_0, U_0). \quad (6)$$

figure 2 shows the first three future DSS as examples. They are calculated from  $a_j(X_0, U_0)$  of each orbit starting from a site  $(X_0, U_0)$  of a fine lattice set on  $D$ . By



**Figure 2.** The future DSS with  $N = 1, 2, 3$ . (Only the first quadrant part shown). The level  $N$  surface consists of altogether  $2^{N+1}$  steps with heights  $\zeta_N^F$  in  $(-1, 1)$ .

definition (6), the level  $N$  surface has  $2^{N+1}$  heights. Now, the examples reveal rather simple structure. Firstly, there is only one *step* for each height in a surface. We call the base of each step a *ribbon* (see figure 3). Then, each ribbon fully extends from  $U_0 = -B$



**Figure 3.** Each step of DSS stands on its own *ribbon*. A PO is illustrated by a ball on its initial point  $(X_0^*, X_0^*)$  and has a height (8). Also shown are the closest step (green), and its base ribbon (blue) enclosing the initial point  $(X_0^*, X_0^*)$ .

to  $U_0 = B$  and there is no isolated bubbles in the base domain. Therefore, the  $2^{N+1}$

ribbons altogether constitute a *tiling* of base domain  $D$ . Furthermore, the height of the step is monotonously increasing, if we traverse ribbons from left to right. Let us describe this as ribbons are *properly tiling*  $D$ .

The reason why the surface is organized in this way at every  $N$  is by no means trivial and we give a proof in section 3. A remark is in order about our approach based on based on finite  $N$  (or coarse-grained) DSS. The edges of ribbons constitute the unstable (stable) manifolds of the collision for the future (past) DSS, because the change of the code is invoked by the collision. (See figure 6). They can be calculated by Gutzwiller's technique of the collision parameter [2]. In a way, our approach is dual to Gutzwiller's. However, the reason of monotonic ordering of the manifolds is very hard to see in the latter. More importantly, the proof on proper tiling (by mathematical induction regarding  $N$ ) in turn clarifies how the higher level surfaces are generated by the repeated application of one-time map. And, through this generating mechanism, we can clarify the coexistence of PO having the same code.

Now, let us consider how a PO is related to ribbons. The code of a PO is cyclic, that is,

$$a_{\text{PO}}^F = (a_0, a_1, \dots, a_{2n-1}; a_{2n} = a_0, a_{2n+1} = a_1, \dots). \quad (7)$$

Here the first  $2n$  bits are the primary part of the PO and the integer  $n$  is the rank of the PO<sup>7</sup>. If the initial point of the PO is  $(X_0^*, U_0^*) \in D$ , its height is naturally defined by

$$\zeta_{\text{PO}}^F(X_0^*, U_0^*) = \frac{1}{1 - \frac{1}{2^{2n}}} \left\{ \sum_{j=0}^{2n-1} \frac{1}{2^{j+1}} a_j(X_0^*, U_0^*) \right\}, \quad (8)$$

where the pre-factor takes care of the repetition of the primary cycle. Then we can prove the following:

*A step of the level  $N$  DSS whose height is given by the first  $N+1$  bits of the string (7);*

$$\zeta_N^F(a) = \sum_{j=0}^N \frac{1}{2^{j+1}} a_j(X_0^*, U_0^*). \quad (9)$$

*is the closest to the PO in height. Therefore, its ribbon traps the initial point  $(X_0^*, U_0^*)$ . See figure 3.*

To see this, consider the amount of misfit between  $\zeta_{\text{PO}}^F$  and  $\zeta_N^F$ . It is nothing but the contribution truncated away from the string (7) under the coarse-graining to level  $N$ . Therefore,

$$\delta \equiv \zeta_{\text{PO}}^F - \zeta_N^F = \sum_{j=N+1}^{\infty} \frac{1}{2^{j+1}} a_j(X_0^*, U_0^*) \quad (10)$$

and we find  $|\delta| \leq 1/2^{N+1}$ . On the other hand, the difference of height between neighboring steps is  $\Delta_N = 1/2^N$ . Therefore, the selected step is the closest.<sup>8</sup> At the

<sup>7</sup> The length of PO must be even ( $2n$ ), because it must cross the  $x$ -axis even times to complete its period.

<sup>8</sup> This statement holds irrespective of whether the tiling by ribbons is proper or not.

large  $N$  limit, the misfit  $\delta$  vanishes and the PO asymptotically sits on the selected step, whether the enclosing ribbon shrinks or not. ■

### 2.3. One-time map

We now investigate the one-time map from a rectangle  $D_0$  on a certain PSS onto  $D_1$  on the next PSS.

$$\begin{aligned} \mathcal{F} : \quad D_0 &\longrightarrow D_1 \\ \Psi &\qquad\qquad \Psi \\ (X_0, U_0) &\longmapsto (X_1, U_1). \end{aligned} \quad (11)$$

This is a challenging problem, because the AKP flow involves both hyperbolic and elliptic singularities. Separation as well as blow up inevitably occur and a brute force numerical integration only is not sufficient to grasp the feature. However, the map restricted to the collision manifold,  $\mathcal{F}|_I$ , is worked out by Gutzwiller in [2]. The Hamiltonian (1) is rewritten using polar coordinates  $(r, \psi)$  and  $(\chi, \vartheta)$  for both the coordinates and momenta;

$$\begin{aligned} x &= r \cos \psi, & u &= \sqrt{\mu} e^x \cos \vartheta, \\ y &= r \sin \psi, & v &= \sqrt{\nu} e^x \sin \vartheta. \end{aligned} \quad (12)$$

The kinetic energy is  $K = e^{2x}/2$  and under the canonical choice of energy  $H = -1/2$  it follows

$$r = 2/(1 + e^{2x}). \quad (13)$$

Slowing down the orbit by  $dt' = e^{3x} dt$ , and taking the limit  $\chi \rightarrow \infty$ , the equation of motion is reduced to an autonomous form <sup>9</sup>

$$\begin{aligned} \frac{d\vartheta}{dt'} &= -(\sqrt{\mu} \cos \vartheta \sin \psi - \sqrt{\nu} \sin \vartheta \cos \psi), \\ \frac{d\psi}{dt'} &= -2(\sqrt{\nu} \cos \vartheta \sin \psi - \sqrt{\mu} \sin \vartheta \cos \psi). \end{aligned} \quad (14)$$

This gives the map

$$\mathcal{M} : (\vartheta_0, \psi_0) \rightarrow (\vartheta_1, \psi_1), \quad (15)$$

where  $(\vartheta_0, \psi_0)$  and  $(\vartheta_1, \psi_1)$  parameterize respectively the initial and final I. ( $\psi_0$  and  $\psi_1$  are either 0 or  $\pi$ , because  $y = 0$  on PSS.  $\psi_0$  is taken to be 0 as a choice of the fundamental initial domain). Thus all we need to obtain  $F_I$  in terms  $(X, U)$  is properly pulling back and pushing forward (15);

$$\mathcal{F}|_I : (X_0, U_0) \xrightarrow{*} (\vartheta_0, \psi_0) \xrightarrow{\mathcal{M}} (\vartheta_1, \psi_1) \xrightarrow{*} (X_1, U_1), \quad (16)$$

where the map with the starred arrow should be calculated by

$$X = 2 \operatorname{sign}(\cos \psi) \cos^2 \vartheta, \quad U = \operatorname{sign}(\cos \vartheta) \frac{\pi \sqrt{\mu}}{2}, \quad (17)$$

<sup>9</sup> The collision occurs at  $\chi = \infty$ . This is equivalent to the blow up technique used by Devaney [16] to remove the singularity due to the collision and introduce the collision manifold. See also McGehee [17].

which is valid on I. The above outline to obtain  $\mathcal{F}_I$  is substantiated in Appendix A. A careful examination is necessary because firstly the initial domain of the map  $\mathcal{M}$  divides into three regions (1, 2, 3) due to the separation by hyperbolic singularities (see the flow in figure A1) and furthermore the pulling back and push forward procedure in (16) introduces additional criticality (when  $\vartheta_0$  passes through  $\pi/2$ , or, when  $\vartheta_1$  passes through  $3\pi/2$ ). Consequently, the collision manifold I is divided eventually into five regions 1, 2A, 2B, 2C, 3 and we have to consider how each is mapped by  $\mathcal{F}_I$ . This issue

**Table 1.** Regions 1, 2, 3 are separated by hyperbolic singularities  $H_v$  and  $H_h$ ;  $\psi_0 = 0$  by definition but  $\psi_1 = 0, \pi, 0$  respectively for 1,2,3. Region 2 is sub-divided by criticalities at  $\vartheta_0 = \pi/2$  and  $\vartheta_1 = 3\pi/2$ .  $X_{v,h,c} = 2 \cos^2(\vartheta_{v,h,c})$  and  $B = 2\pi\sqrt{\mu}/2$ .

	$\vartheta_0(\psi_0 \equiv 0)$	$\vartheta_1$	$\psi_1$	$X_0$	$U_0$	$X_1$	$U_1$
1	$0 \rightarrow \vartheta_v$	$0 \rightarrow -\vartheta_h$	0	$2 \rightarrow X_v$	$B$	$2 \rightarrow X_h$	$B$
$\Updownarrow$	$\vartheta_v$	Separation by $H_v$					
2A	$\vartheta_v \rightarrow \frac{\pi}{2}$ $\frac{\pi}{2} \spadesuit$	$\pi + \vartheta_h \rightarrow \pi + \vartheta_c$ $(\pi + \vartheta_c)$	$\pi$	$X_v \rightarrow 0$	$B$	$-X_h \rightarrow -X_c$	$-B$
2B	$\frac{\pi}{2} \rightarrow \pi - \vartheta_c$ $(\pi - \vartheta_c)$	$\pi + \vartheta_c \rightarrow \frac{3\pi}{2}$ $\frac{3\pi}{2} \clubsuit$	$\pi$	$0 \rightarrow X_c$	$-B$	$-X_c \rightarrow 0$	$-B$
2C	$\pi - \vartheta_c \rightarrow \pi - \vartheta_h$	$\frac{3\pi}{2} \rightarrow 2\pi - \vartheta_v$	$\pi$	$X_c \rightarrow X_h$	$-B$	$0 \rightarrow -X_v$	$B$
$\Updownarrow$	$\pi - \vartheta_h$	Separation by $H_h$					
3	$\pi - \vartheta_h \rightarrow \pi$	$\pi + \vartheta_v \rightarrow \pi$	0	$X_h \rightarrow 2$	$-B$	$X_v \rightarrow 2$	$-B$

- $\spadesuit$   $\vartheta_0$  crosses  $\frac{\pi}{2}$  from below inducing  $U_0 : B \rightarrow -B$ .  
 $\clubsuit$   $\vartheta_1$  crosses  $\frac{3\pi}{2}$  from below inducing  $U_1 : -B \rightarrow B$ .

is discussed in Appendix A and the result is summarized in table 1 above. Figure 4 is graphical representation of it. We observed that (i) the boundary map  $\mathcal{F}|_I$  acts on the

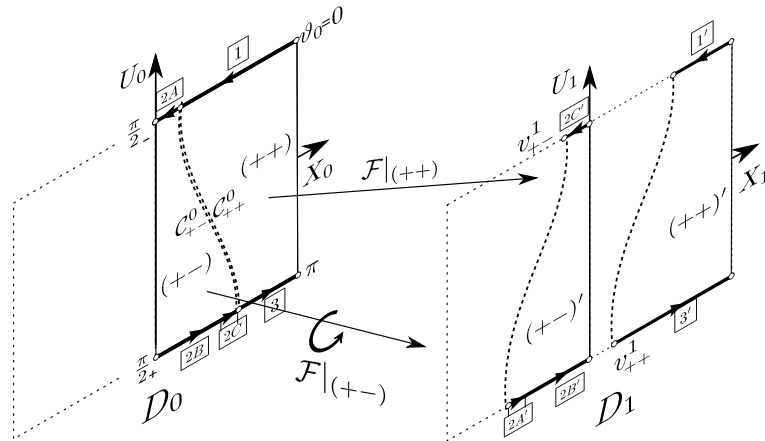


**Figure 4.** Boundary map  $\mathcal{F}|_I$  given by table 1. Full map  $\mathcal{F}$  sends  $(++)$  and  $(+-)$  to the left and right respectively; besides, the boundary of  $(+-)$  is ‘rotated’.  $C_{+\pm}^0$  are mapped not onto boundary curves of  $(\pm\pm)'$ , but into the end points  $v_{\pm\pm}^1$  respectively.



boundaries of  $(++)$  and  $(+-)$  separately, sending them to the left and right respectively, and that (ii)  $\mathcal{F}|_{(+-)}$  rotates the boundary of  $(+-)$  by one sub-region.

The virtue of the collision manifold analysis is that  $\mathcal{F}|_I$  extends to the interior and helps to grasp the behavior of the internal map  $\mathcal{F}$ —the point emphasized by Devaney [16]. In figure 5, we combine figure 4 with the numerically calculated interior

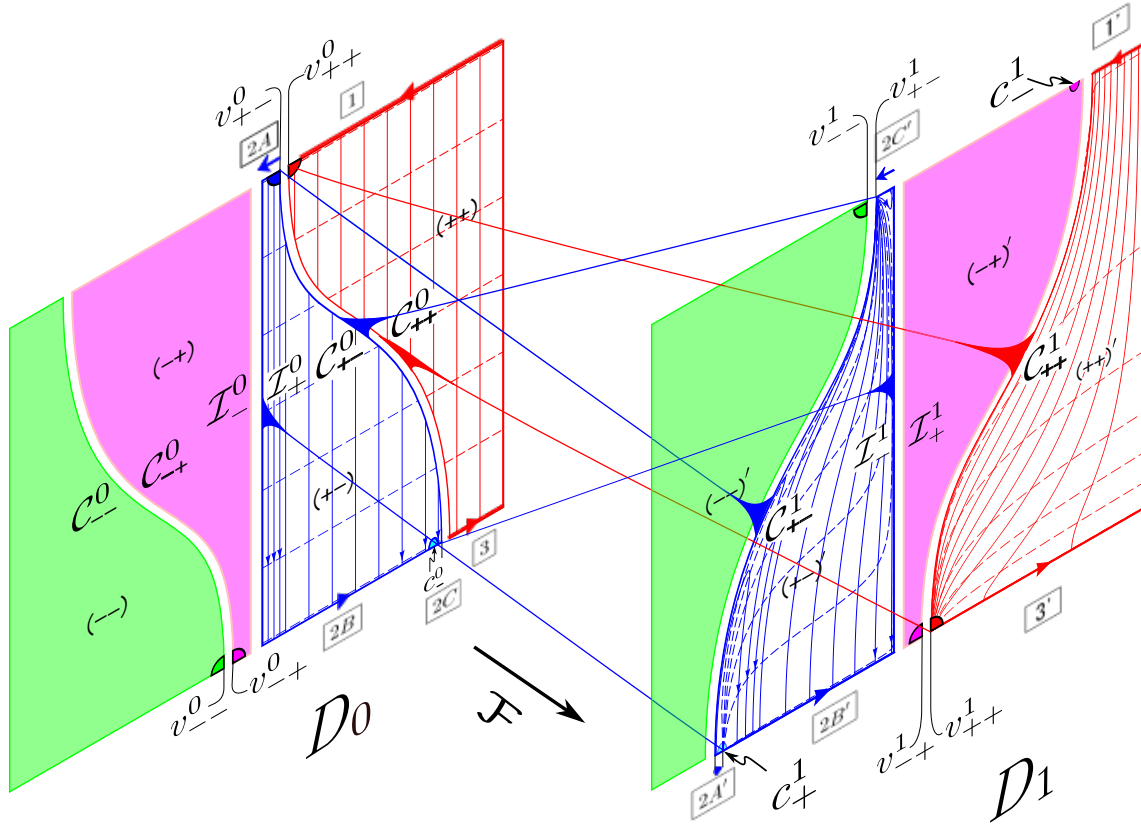


**Figure 5.** Critical maps (B.1)–(B.5). Connectors of criticalities are shown only on the boundaries of  $(++)$  and  $(+-)$ .  $\gamma = 0.2$  and to scale.

map. Indeed above two characteristics  $\mathcal{F}|_I$  clearly controls the interior map. The middle regions  $(+-)$  and  $(-+)$  swaps the order to become  $(-+)'$  and  $(+-)'$  in the image corresponding to the separation property (i) of  $\mathcal{F}|_I$ . Remarkably, the distortion of the orthogonal lattice in  $D_0$  shows that there exist focus points in the interior map, for instance,  $v_{++}^1$  and  $v_{+-}^1$ , which are respectively the image of the sides of the separator curve  $C$ .

$$\begin{aligned} C_{++}^0 &\rightarrow v_{++}^1, \\ C_{+-}^0 &\rightarrow v_{+-}^1. \end{aligned}$$

For the notation of critical objects, see Appendix B. Furthermore, the rotation property (ii) implies that the vertical lines connecting  $2A$  and  $2B$  in  $D_0$  must be bent to connect the images  $2A'$  and  $2B'$  both in the bottom boundary of  $D_1$ . This produces wing-shaped curves in  $D_1$  showing folding property in  $\mathcal{F}$ . The wings contract to a single point  $c_+^0$ , and it is as well a focus point to which the  $X_0 = 0$  ends of horizontal lines in  $(+-)$ , namely  $\mathcal{I}_+$ , are mapped;

$$\mathcal{I}_+ \rightarrow c_+^1.$$

We investigate these phenomena accurately in Appendix B. The occurrence of blow-up and contraction may appear ad-hoc, but it is quite systematic. This can be seen if we follow in table 1 the seven parts in the boundary of  $(+-)$  (and their image) counter-clockwise;

$$\begin{array}{cccccccc}
 v_{+-}^0 & \rightarrow & 2A & \rightarrow & \mathcal{I}_+^0 & \rightarrow & 2B & \rightarrow & c_-^0 & \rightarrow & 2C & \rightarrow & C_{+-}^0 \\
 0 & & l_v & & \ell(\mathcal{I}) & & l_c & & 0 & & l_h - l_c & & \ell(C) \\
 \wedge & & & & \vee & & & & \wedge & & & & \vee \\
 C_{+-}^1 & \rightarrow & 2A' & \rightarrow & c_+^1 & \rightarrow & 2B' & \rightarrow & \mathcal{I}_-^1 & \rightarrow & 2C' & \rightarrow & v_{+-}^1 \\
 \ell(C) & & l_h - l_c & & 0 & & l_c & & \ell(\mathcal{I}) & & l_v & & 0.
 \end{array} \tag{18}$$

Here  $\ell(C)$  and  $\ell(\mathcal{I})$  denote respectively the length of the separator curve  $C$  and  $\mathcal{I}$ . ( $\ell(\mathcal{I}) = \pi\sqrt{\mu}$ ,  $l_{v,h,c} = 2\cos^2\vartheta_{v,h,c}$ ). The blow-up and contraction of a part are specified by  $\wedge$  and  $\vee$  symbols respectively. Note  $(+-)$  and  $(+-)'$  are congruent each other, because  $(+-) = P(T((+-)'))$ , see (C.5). Indeed the blow-up and contraction are involved symmetrically equal-times so that the perimeters of  $(+-)$  and  $(+-)'$  are intriguingly kept the same. The reason why a curve is contracted into a point and a

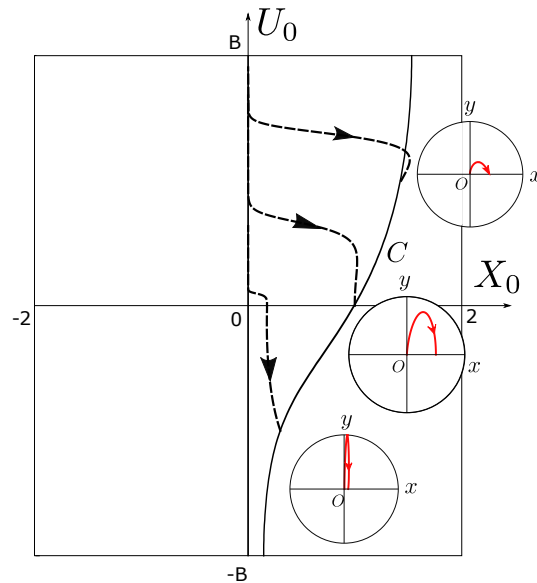


**Figure 6.** Three collision orbits in circles, and their projection in  $(X, U)$  plane (dashed curves). The latter reach the separator curve  $C$  at the first arrival at the PSS.

point is blown up to a curve is as follows. In figure 6, we show the result of our collision parameter analysis, which follows Gutzwiller [5, 7]. The collision orbits are created as a one parameter family. parameter  $A$ . The first short time interval is analytically calculated and continued by numerical integration. The positions of the first arrivals on the Poincaé surface forms a curve in the  $(X_1, U_1)$ -rectangle developed by the parameter  $A$ . This is nothing but the separator curve  $C$ . This is a typical sample of the blow-up process. Note that one can reversely track back by numerical integration (with slow down) starting from  $C_{+-}^1$ , but it is difficult to follow their motion after closely reaching the upper end of  $\mathcal{I}$ .

Continuing numerically the collision trajectory for many crossings of PSS, the stable and unstable manifold are produced as shown in Gutzwiller Fig.2 in [2] and Fig.26 in [5]. In a way, our approach and collision analysis are complementary to each other. We focus on finite  $N$  ribbons, while the collision analysis focuses on inter-ribbon-ribbon curves. That is, the longitudinal line separating two ribbons are nothing but the stable/unstable manifold, because the code change is just induced by the collision. The difference is that, while it is a tough problem in the collision parameter analysis to tell which hierarchy a line is subject to, our approach has the advantage of a simple book-keeping. Hence it can be easily used to locate PO directly, and helps to resolve the coexistence of stable and unstable POs of the same code. We discuss these points in detail below.

### 3. Creation Mechanism of Proper Tiling by Ribbons

#### 3.1. Proper Tiling by Ribbons of the Initial value Domain $D_0$ . Proof Starts:

We prove below that

*At any  $N$ , the ribbons are tiled properly*

by mathematical induction with respect to  $N$ . The  $N = 0$  case is special and the one-time-map scheme in figure 5 is responsible for  $N \geq 1$ . The future case is considered; past case goes similarly. In the proof it is clarified how level  $N + 1$  tiling is created from level  $N$ , and this in turn shows how a non-shrinking ribbon can appear in a special case.

$N = 0$ : The  $N = 0$  tiling is determined by  $a_0 = \text{sign}(X_0)$ . The ribbons are  $(-)$ ,  $(+)$  from left and right, and the step height  $\zeta_{N=0}^F$  is respectively  $-\frac{1}{2}$ ,  $\frac{1}{2}$ . Therefore, the tiling is proper. Here, the part  $\mathcal{I}_{\pm}^0$  of the collision manifold ( figure 5) takes the role of the separator.

$N = 1$ : Now,  $a_1$  is determined by the separator curves  $C_{++}^0$  and  $C_{--}^0$  in the one-time map  $\mathcal{F}$ . As the result, the height distribution over the ribbons is

$$\begin{array}{cccc}
 \zeta^{N=1} & -\frac{3}{4} & -\frac{1}{4} & \frac{1}{4} & \frac{3}{4} \\
 & \uparrow & \uparrow & \uparrow & \uparrow \\
 \text{Ribbon : } (a_0, a_1) : & (--) & (-+) & (+-) & (++) \\
 & L \dots & \dots & \dots & \dots R
 \end{array} \tag{19}$$

Each ribbon extends from top to bottom ( $U_0 = B$  to  $-B$ ). Thus, the tiling at  $N = 1$  is also proper.

$N$  to  $N + 1$ : Let us show that, if the level  $N$  tiling of  $(X_0, U_0)$  is proper, then the level  $N + 1$  tiling is also proper for  $N \geq 1$ . The former is determined by (6) by  $(N + 1)$ -bit binary sequence  $(a_0, a_1, \dots, a_N)$ . Let us make the initial value dependence of  $\zeta^N$  via  $\mathcal{F}$  explicit, that is,

$$\zeta^N(X_0, U_0) = \sum_{j=0}^N \frac{(s \circ \mathcal{F}^j)(X_0, U_0)}{2^{j+1}}, \quad (X_0, U_0) \in D_0 \quad (20)$$

where  $s$  is a function

$$s(X, U) \equiv \text{sign}(X).$$

In the same way,  $\zeta^{N+1}(X_0, U_0)$  is by definition calculated from the  $(N + 2)$ -bit sequence  $(a_0, a_1, \dots, a_N, a_{N+1})$ . But the last bit

$$a_{N+1}(X_0, U_0) = (s \circ \mathcal{F}^{N+1})(X_0, U_0)$$

can be only calculated via the full  $\mathcal{F}^{N+1}$ ; it cannot be obtained by simply combining the one-time map  $\mathcal{F}$  with the given level  $N$  height function  $\zeta^N(X_0, U_0)$ . One may resort to a numerical calculation, but then the analytic understanding of the system is lost. A crack of nutshell is to call up the inverse of  $\mathcal{F}$ , and map once *backward* from  $D_0$  onto  $D_{-1}$  to obtain

$$a_{-1} = \text{sign}(X_{-1}) = (s \circ \mathcal{F}^{-1})(X_0, U_0). \quad (21)$$

Then, one can obtain the necessary  $(N + 2)$ -bit sequence  $(a_{-1}, a_0, a_1, \dots, a_N)$  and then examine if the corresponding level  $N + 1$  height function  $\zeta^{N+1}(X_{-1}, U_{-1})$  gives a proper tiling. It is actually a tiling on  $D_{-1}$ , but, from time-shift symmetry, it is equally a tiling on  $D_0$ . Let us calculate it explicitly;

$$\begin{aligned} \zeta^{N+1}(X_{-1}, U_{-1}) &\equiv \sum_{j=0}^{N+1} \frac{s \circ \mathcal{F}^j(X_{-1}, U_{-1})}{2^{j+1}} \\ &= \frac{1}{2} s(X_{-1}, U_{-1}) + \sum_{j=0}^N \frac{s \circ \mathcal{F}^j(\mathcal{F}(X_{-1}, U_{-1}))}{2^{j+2}} \\ &= \frac{1}{2} \text{sign}(X_{-1}) + \frac{1}{2} \zeta^N(X_0, U_0), \end{aligned} \quad (22)$$

where, at the second line,  $j \rightarrow j - 1$  is applied for the sum variable, and the third line is obtained by (20). Now, to prove (22) keeps the properness of tiling, we have clarify how  $\mathcal{F}^{-1}$  acts on the ribbons on  $D_0$ .

The level  $N$  tiling is made of altogether  $2^{N+1}$  ribbons. Let us label them by  $k$  from

left to right so that the left and right-half of  $D_0$  are tiled respectively as<sup>10</sup>

$$\begin{aligned} D_0^- &= \sum_{k \in \Lambda_-} T_k, \quad \Lambda_- \equiv \{1, \dots, 2^N\}, \\ D_0^+ &= \sum_{k \in \Lambda_+} T_k, \quad \Lambda_+ \equiv \{2^N + 1, \dots, 2^{N+1}\}. \end{aligned} \quad (23)$$

The height  $\zeta^N$  has a common value for any  $(X_0, U_0)$  within a ribbon. Hence, it can be regarded as a class function considering a ribbon as an equivalent class of initial points with the same step-height: we write the height of a ribbon  $T_k$  as  $\zeta^N(T_k)$ . The properness of level  $N$  tiling is  $\zeta^N(T_1) < \zeta^N(T_2) < \dots < \zeta^N(T_{2^{N+1}})$  and allowing the extended use of a function on a set  $(f(\{x_1, \dots, x_N\}) = \{f(x_1), \dots, f(x_N)\})$  to a class function,

$$\begin{aligned} \zeta^N[D_0^-] &\equiv \{\zeta^N(T_k)\}_{k \in \Lambda_-} \subset (-1, 0), \\ \zeta^N[D_0^+] &\equiv \{\zeta^N(T_k)\}_{k \in \Lambda_+} \subset (0, +1). \end{aligned} \quad (24)$$

In figure 7, the scheme of  $\mathcal{F}^{-1}$  is laid over the level  $N$  tiling of  $D_0$ . To account for

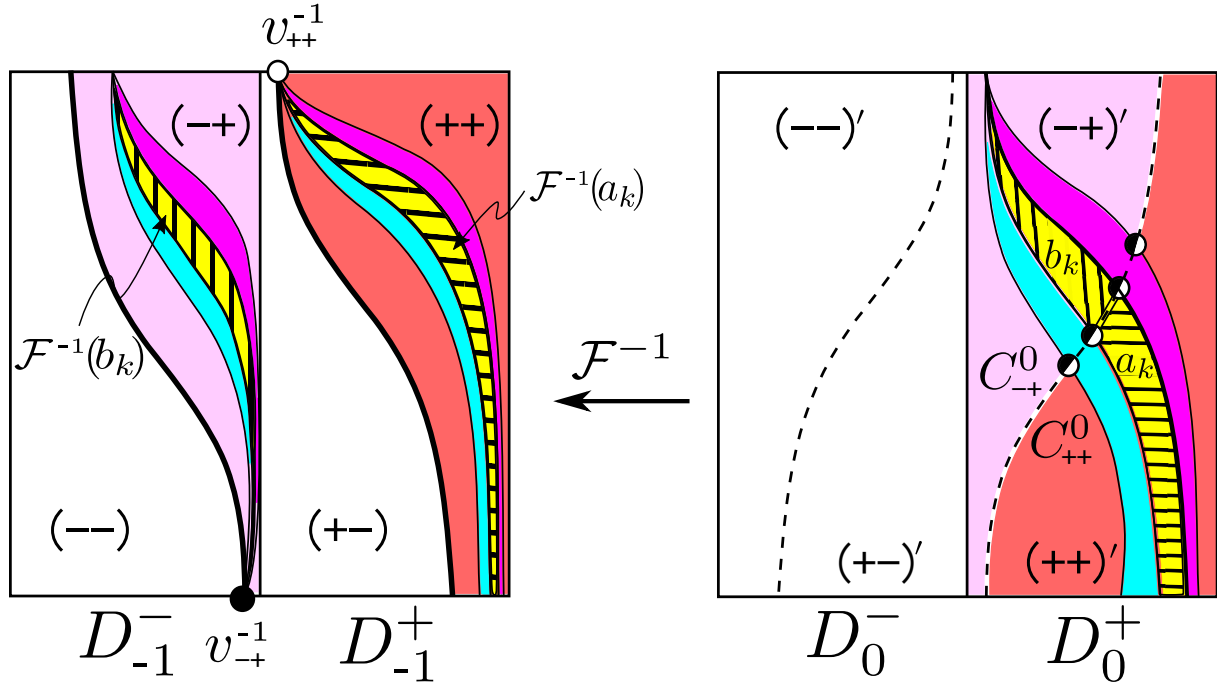


**Figure 7.** The separator  $C_{\pm+}^0$  in  $\mathcal{F}^{-1}$  (figure 5) chops a ribbon in  $D_0^+$ . Since  $C_{\pm+}^0 \rightarrow v_{\pm+}^{-1}$ ,  $a_k$  ( $b_k$ ) is mapped backwards into  $(++)$  [ $(-+)$ ] forming a full height ribbon with vertex  $v_{++}^0$  ( $v_{-+}^0$ ); number of ribbons are doubled. Meant to illustrate a general case, but data with  $\gamma = 0.2$ ,  $N = 3$  is used.

the backward time shift ( $D_{1,0} \rightarrow D_{0,-1}$ ) from figure 5, critical objects are respectively renamed as  $v_{\pm+}^{-1}$  and  $C_{\pm+}^0$ . But, labels for four regions are kept so that  $(+\pm)' \equiv \mathcal{F}[(+\pm)]$  (and  $(+\pm) \equiv \mathcal{F}^{-1}[(+\pm)']$ ).

<sup>10</sup> By time reversal symmetry (Appendix C), the tiling of  $D_0^+$  and  $D_0^-$  are symmetric each other under  $(X, U) \rightarrow (-X, -U)$ .

### 3.2. DSS creation mechanism

We consider ribbons  $T^k, k \in \Lambda_+$  in  $D_0^+$ .

- (i) Each ribbon  $T_k$  is divided by the separator curve  $C_{\pm+}^0$  into sub-parts  $a_k \subset (++)$  and  $b_k \subset (-+)$ , and by the separation property of  $\mathcal{F}^{-1}$ ,  $\mathcal{F}^{-1}(a_k) \subset (++) \subset D_{-1}^+$  and  $\mathcal{F}^{-1}(b_k) \subset (-+) \subset D_{-1}^-$ . Because  $C_{\pm+}^0 \rightarrow v_{\pm+}^{-1}$ , all  $\mathcal{F}^{-1}(a_k)$  ( $\mathcal{F}^{-1}(b_k)$ ) have top point at  $v_{++}^{-1}$  (bottom point  $v_{-+}^{-1}$ ) and, as a whole, tiles  $(++)$  [ $(-+)$ ]. Every ribbon is elongated to full height (from  $U_0 = -B$  to  $+B$ ), and the number of ribbons is in this way doubled.
- (ii) Because  $\mathcal{F}^{-1}$  is orientation-preserving, the order of ribbons are maintained region by region. Therefore, the properness of tiling of  $(\pm+)$ ' inherits to  $(\pm+)$ .
- (iii) Because  $\mathcal{F}^{-1}$  is area-preserving, it holds (denoting the area of  $T_k$  as  $S(T_k)$ )

$$\begin{aligned} S(T_k) &\equiv S(a_k) + S(b_k) = S(\mathcal{F}^{-1}(a_k)) + S(\mathcal{F}^{-1}(b_k)) \\ &\implies S(T_k) \geq S(\mathcal{F}^{-1}(a_k)), S(\mathcal{F}^{-1}(b_k)). \end{aligned} \quad (25)$$

But the height of ribbons  $\mathcal{F}^{-1}(a_k)$ ,  $\mathcal{F}^{-1}(b_k)$ , and  $T_k$  are all equal, (25) implies that the created ribbons are in general finer than their parent. This is case (A) referred in the introduction. However, there is a remarkable exception;

$$S(\mathcal{F}^{-1}(a_k)) = 0 \implies S(T_k) = S(\mathcal{F}^{-1}(b_k)). \quad (26)$$

This is the case (B), leading to the Broucke-type stable PO in a non-shrinking ribbon. This point is further examined in section 4.2 below.

### 3.3. Step-Height Distribution and End of the Proof

Applying  $\zeta^{N+1}$  in (22) on the region  $(a_0, a_1) \subset D_{-1}$  as an extended class function (acting every ribbon inside the region  $(a_0, a_1)$ ), we obtain

$$\zeta^{N+1}[(a_0, a_1)] = \frac{1}{2}s[(a_0, a_1)] + \frac{1}{2}\zeta^N[\mathcal{F}[(a_0, a_1)]] \quad (27)$$

For all ribbons inside  $(a_0, a_1)$ , the sign of  $X_{-1}$  is  $a_0$ , so the first term is simply  $a_0/2$ . (The term  $a_{-1}$  in (21) implies  $\text{sign}(X_{-1})$ ). In the second term,

$$\mathcal{F}[(a_0, a_1)] \subset \begin{cases} D_0^+ & \text{if } a_1 = +1 \\ D_0^- & \text{if } a_1 = -1, \end{cases}$$

and via (24),

$$\zeta^N(\mathcal{F}[(a_0, a_1)]) \subset \begin{cases} (0, 1) & \text{if } a_1 = +1 \\ (-1, 0) & \text{if } a_1 = -1, \end{cases}$$

or, in one line,

$$\zeta^N(\mathcal{F}[(a_0, a_1)]) \subset \frac{a_1}{2} + \left(-\frac{1}{2}, \frac{1}{2}\right). \quad (28)$$

Therefore, (27) gives

$$\zeta^{N+1}[(a_0, a_1)] \subset \frac{a_0}{2} + \frac{a_1}{2^2} + \left(-\frac{1}{4}, \frac{1}{4}\right). \quad (29)$$

The distribution of height is

$$\begin{array}{cccc} \zeta^{N+1} \subset & (-1, -\frac{1}{2}) & (-\frac{1}{2}, 0) & (0, \frac{1}{2}) & (\frac{1}{2}, 1) \\ & \uparrow & \uparrow & \uparrow & \uparrow \\ D_0 \text{ region} & (--) & (-+) & (+-) & (++) \\ & L \dots & \dots & \dots & \dots R \end{array} \quad (30)$$

The ribbon tiling inside each region is proper due to item (ii) of the creation mechanism, and now (30) shows the range distribution over regions is also proper. Therefore, the level  $N + 1$  tiling is proper. ■

A remark: We see clearly that, dropping the last term  $(-1/4, 1/4)$ , it gives the basic height distribution of  $N = 1$  tiling in (19).

#### 4. Stable and Unstable Periodic Orbits in AKP

##### 4.1. Use of Ribbons to Locate the Initial Point of a Periodic Orbit

In section 2.2 we have shown that, for a given periodic binary code in (7), the initial point  $(X_0^*, U_0^*)$  of corresponding PO should be enclosed in the level  $N$  ribbon, whose step has the height of the first  $N + 1$  bits of the code and this holds at any  $N$ . The same is true for the past case. And future and past tiling are in general transverse each other (see Appendix C). Therefore, the initial point  $(X_0^*, U_0^*)$  should be inside the junction of responsible future and passed ribbons. Furthermore, in section 3, we have proved that the tiling is properly ordered by the height. Therefore, it is possible to locate the appropriate ribbon by its height and we can locate PO-initial-point  $(X_0^*, U_0^*)$  inside a junction of corresponding future and past ribbons with no mistake.

But now, one must carefully examine whether at large  $N$ , all ribbons shrink to vanishing width, case (A), or some ribbon escapes from shrinking. case (B). See (iii) in section 3.2 above.

Case (A) appeals naive intuition—some part of a ribbon is definitely chopped away by the separator, it would then loose the area. As the elongation keeps its height as before, it would become thinner. At large  $N$ , the junction enclosing the  $(X_0^*, U_0^*)$  would converge to a point and the initial point would be singled out<sup>11</sup>. Figure 8 in fact corresponds to this case. However, even though case (B) looks pathological, it really occurs and it is the origin of Broucke's stable orbits in AKP. Here, each ribbon is indeed chopped by the separator and resultant two parts are elongated back to the full length. But, it can occur that one part can have full area and the other none after the chopping. This can occur when the latter has already shrunk to a line segment! The separator can

<sup>11</sup> And even the uniqueness of the PO with a given code would be proved. This argument is indicated as a possibility in [7].

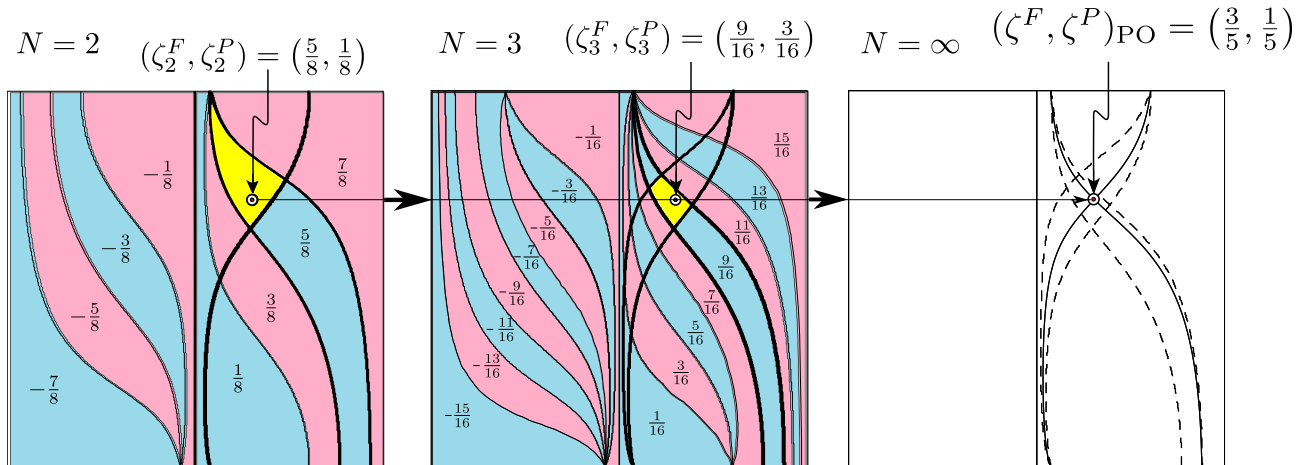


**Figure 8.** Ribbon-evolution at  $\gamma = 0.2$ . All future ribbons and one past ribbon relevant for the PO are shown, and the overlap is highlighted. The PO (shown by circle dot) is code  $(++--)$ , (rank 2, Id=3).  $(\zeta^F, \zeta^P) = (3/5, 1/5)$  by (8). The overlap is with heights  $(5/8, 1/8)$   $((9/16, 3/16))$  at  $N = 2$  ( $N = 3$ ) by (6).

then only cut out measure zero area, and the survivor remains with finite area. This is so subtle, but the consequence is crucial. It gives a room for a stable PO survives in AKP. We are amazed that such an exception leads to physically basic phenomenon.

## 4.2. Advent of Stable Periodic Orbits

**4.2.1. Stable periodic orbits and non-shrinking ribbon** Now, let us show how the non-shrinking ribbon occurs taking the case of Broucke's PO as a good example. Broucke reported two *stable* POs, and here we take the shorter one; it is rank  $n = 3$  with the code  $(+--+-)$ . We call it 'Broucke's stable PO3-6'.<sup>12</sup> We show in figure 9 how the future ribbons evolve with the increase of  $N$ .

The top row shows tiling  $T_6, T_{12}, T_{42}$ . In each, three particular ribbons are shown, namely the ribbon which encloses the initial point  $(X_0^*, U_0^*)$  of the Broucke's PO (we call it Broucke's ribbon and give a mark 'B'), and two neighboring ones. Remarkably only the Broucke's ribbon survives, while other diminishes rapidly with width  $\sim 1/2^N$ . In the first column  $T_6 \rightarrow T_7 \rightarrow T_8$  ( $N \pmod 6 = 0, 1, 2$ ), we clearly observe the process that (i) each ribbon is chopped by the separator curve into two parts, (ii) one is sent to the left and the other to the right half of the rectangle, and (iii) each is stretched between upper and lower boundary. As a result, duplication of full-height ribbons occurs, each finer than its parent roughly by half. Now, in the second column starting  $T_{12}$ , the separator curve is chopping out only very fine ribbon near the bottom! Further in the third column, the separator is now inactive—chopping out only a line segment. *The non-shrinking ribbon is protecting itself from shrinkage by changing its tail to a line at early stage.* The same occurs for the past Broucke's ribbon. Therefore, the overlap

<sup>12</sup> The *unstable* periodic orbit with the same code had been given an identification number '-6' among rank 3 distinct POs by Gutzwiller in his PO classification scheme [4].



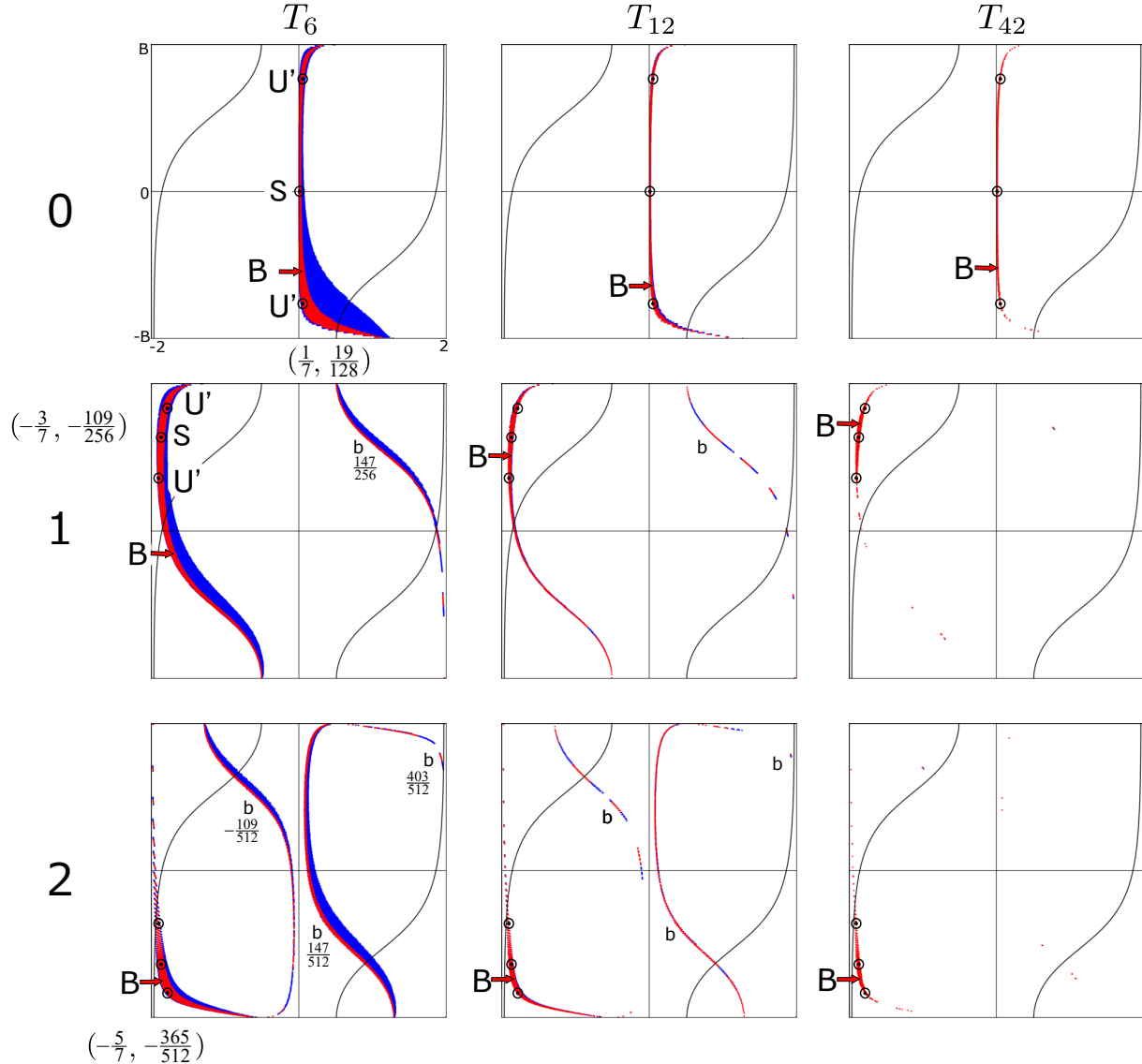


**Figure 9.** Evolution of future ribbons of Broucke's PO3-6. Snap shots of tiling  $T_N$  at  $N = (6, \dots, 44)$  with  $T \pmod{6}$ .  $\gamma = 0.611$ . Circle-dots: ( $S$ ) and unstable ( $U'$ ) PO. 'B': the ribbon enclosing them ('b' chopped away parts). 'B' remains non-shrinking, while adjacent-side ribbons vanish quickly. Heights  $(\zeta_{\text{PO}}^F(X_0^*, U_0^*), \zeta_N^F(a))$  as given by (8), (9).  $\zeta_N^F(a)$  can be also calculated by (27), e.g. comparing  $T_6$  and  $T_8$ ,  $-\frac{365}{512} = -\frac{1}{2} + \frac{1}{2}(-\frac{1}{2} + \frac{1}{2} \cdot \frac{19}{128})$ . Initial positions of POs in  $T_0$  are for canonical reading of code as  $(a_0, \dots, a_5) = (+ - - + --)$ ; those in  $T_N$  are given by acting  $(\mathcal{F}^{-1})^N$ .

of Broucke's future and past ribbons constitutes finite-size domain around the initial point  $(X_0^*, U_0^*)$ , and any orbit starting from a point inside the neighborhood evolves producing the same code with the Broucke's PO forever in both the future and the past. The Broucke's PO in the center is a stable PO in itself.

4.2.2. *The bifurcation process  $U \rightarrow S + U'$ ; threshold behavior* Now let us follow the decrease of the anisotropy by increasing  $\gamma$  and investigate how the Broucke stable PO3-6 comes out. As shown in figure 10, there is a threshold  $\gamma_{th}$  where the unstable PO ( $U$ ) changes into the stable one ( $S$ ) following the advent of non-shrinking ribbons enclosing  $S$ . At the same time, a new unstable PO ( $U'$ ) is born. Thus the stable PO emerges in a bifurcation process  $U \rightarrow S + U'$ . All of the POs ( $U, S, U'$ ) in the process are symmetric

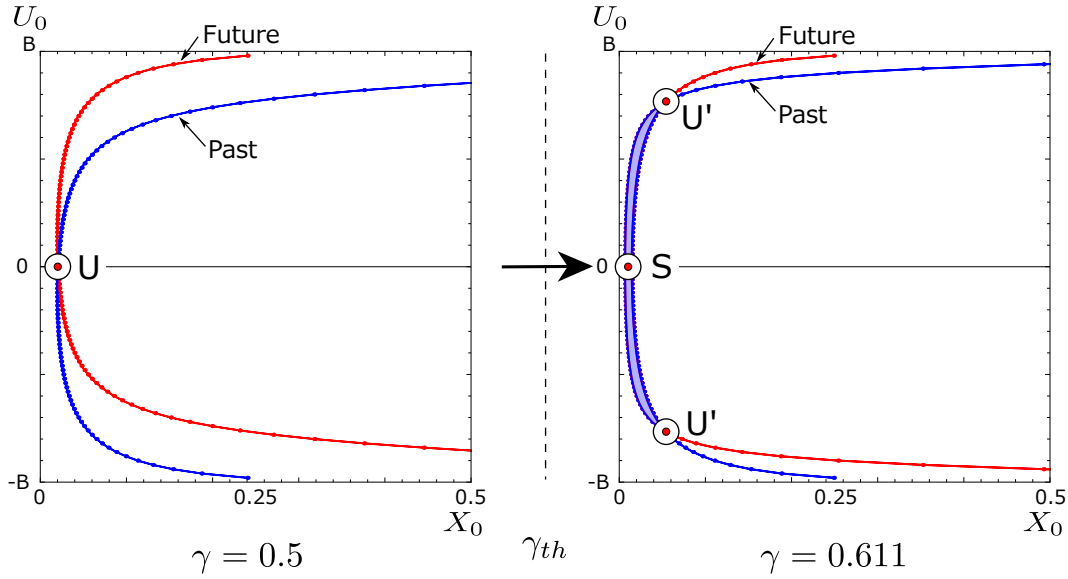


**Figure 10.** The transition process  $U \rightarrow S + U'$ . The ribbons are calculated at asymptotic  $N$  ( $N = 48$ ). Left:  $\gamma = 0.5$ . Right:  $\gamma = 0.611$ . ( $\gamma_{th} = 0.572350895$  for the Broucke's PO3-6). The two  $U'$ 's are the appearance of the same PO at different time slices ( $T = 45$  and  $T = 48$ ).

under the  $Y$  transformation

$$Y : x \rightarrow x, y \rightarrow -y.$$

The bifurcation proceeds in the following way.

(1) Below the threshold, both future (F) and past (P) ribbons have shrunk to curves at the asymptotic  $N$  and they mutually cross each other at a single point on the  $U_0 = 0$  line<sup>13</sup>.  $U_0 = 0$  implies  $p_x = 0$ , and the orbit perpendicularly crosses the  $x$ -axis at, say,  $(X_0, U_0) = (X_0^*, 0)$ . Thus, the orbit is symmetric under  $Y$ -transformation. Now, an infinitesimal shift from  $(X_0^*, 0)$  leads to the slip off from the crossing point of F and P ribbons; thus disables the orbit to repeat the code of PO. This is the way the PO ( $U$ ) is unstable in terms of ribbons below the threshold.

(2) Right on the threshold, the F and P ribbons become tangent each other at  $U_0 = 0$ .

(3) Above the threshold the ribbons stop shrinking and they start extending an overlap around  $U_0 = 0$ . See figure 11. Inside the overlap, the orbit can repeat the sequence in

<sup>13</sup> Precisely, as in figure 9, a PO (and F, P ribbons enveloping it) evolve periodically in  $D_0$ , but at  $T_N$  ( $N \equiv 0 \pmod{2n}$ ), the maximum overlap comes at  $U_0 = 0$ .

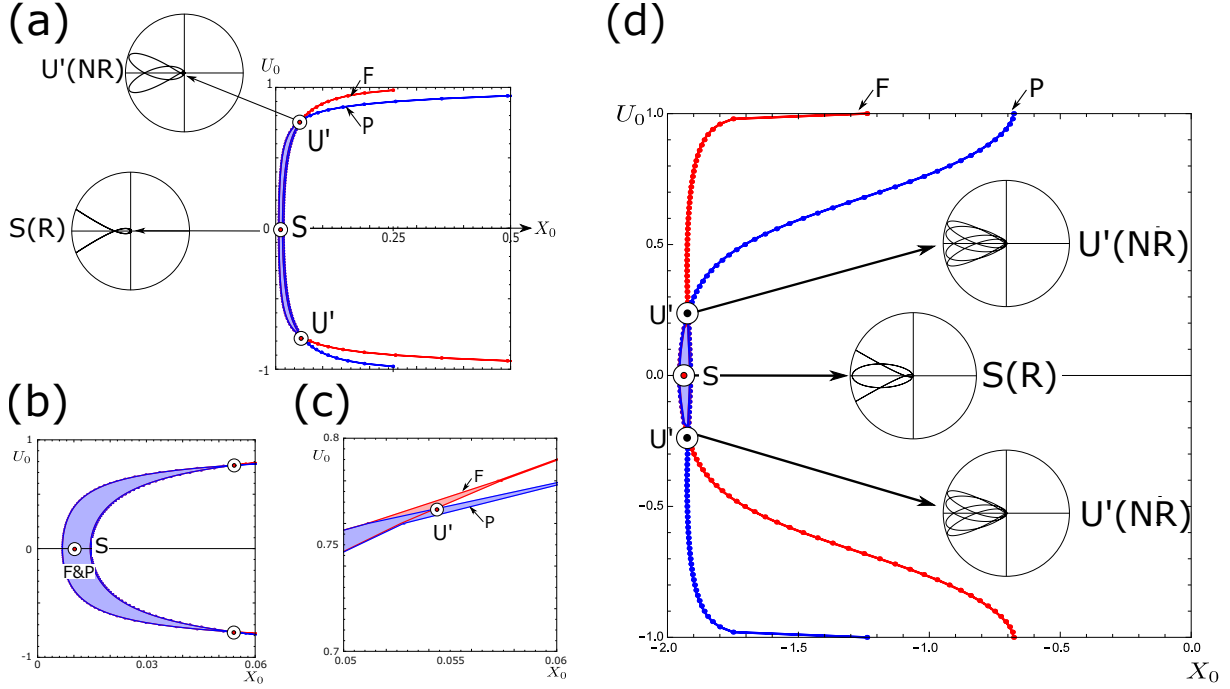


**Figure 11.** Broucke PO bifurcates as  $U(R) \rightarrow S(R) + U'(NR)$ . Initial points of Broucke's POs after the bifurcation are shown in the overlap of future (red) and past (blue) ribbon at level  $N = 48$ . (a-c) PO3-6 ( $\gamma = 0.611$ ), (d) PO5-40 ( $\gamma = 0.77$ ).  $S(R)$  and  $U'(NR)$  respectively locate in the maximum overlap and at edge of the overlap. See magnified figures (b), (c) for PO3-6. Insets show  $N$  and  $NR$  orbit profiles.

both future and past. The previously unstable orbit ( $U$ ) becomes stable ( $S$ ) remaining at  $U_0 = 0$ . Therefore  $S$  is also  $Y$ -symmetric. The initial point of the new-born PO ( $U'$ ) locates at the corner of the overlap so that a slight shift again (as was the case of  $U$ ) leads to the slip off from the overlap. It realizes instability still keeping periodicity in this way. It is remarkable that it is also  $Y$ -symmetric even though  $U_0$  is not vanishing now. This is no contradiction since  $U_0 = 0$  is a sufficient condition for the PO to be  $Y$ -symmetric but it is not a necessary condition. Indeed, we show below that  $U'$  belongs in a different symmetry class (self-non-retracing) from that of  $U$  and  $S$  (self-retracing). We add that there is no other PO of the same code within the overlap. For detail, see Appendix E.

**4.2.3. Lyapunov exponents** The change of the maximum Lyapunov exponent of Broucke PO is shown in the bifurcation diagram in figure 12. We can now follow the transition process through  $\gamma = 0.1$ — $0.8$ . We observe the followings.

- (1) Above  $\gamma_{th}$ , both stable and unstable orbit of the same code co-exist. As the associated orbit profiles clearly shows, the PO in the stable branch is self-retracing (the same with the unstable PO below  $\gamma_{th}$ ), while that in the unstable branches

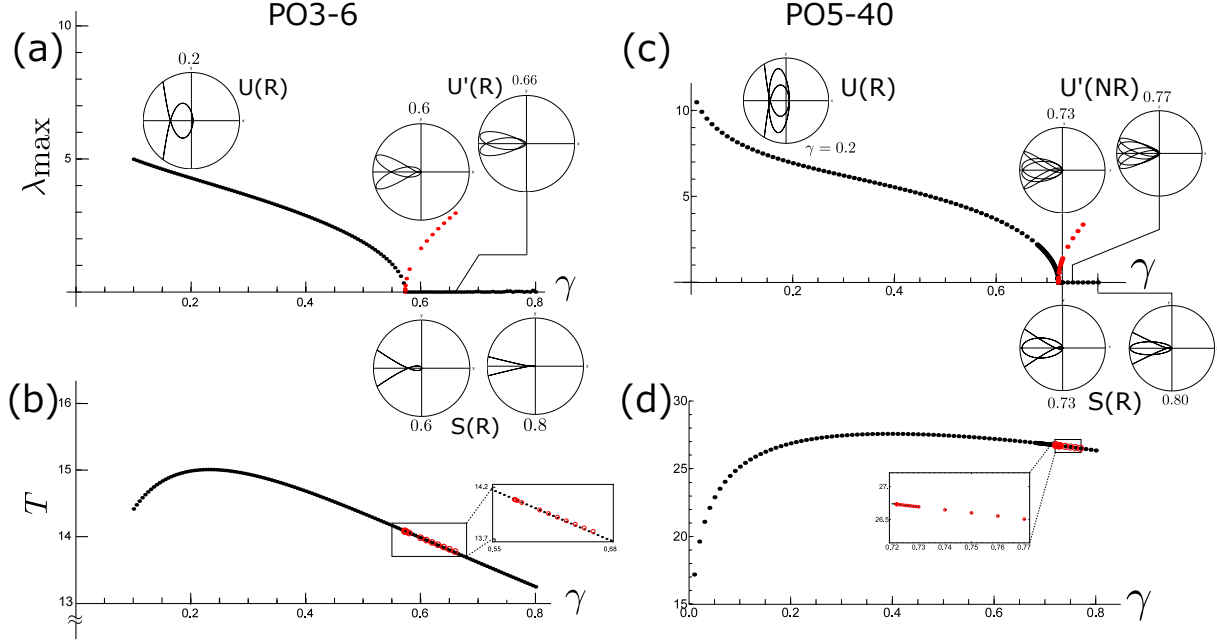


**Figure 12.** Bifurcation of (a-b) PO3-6 and (c-d) PO5-40. Both  $U(R) \rightarrow S(R) + U'(NR)$ . The retracing orbit, perpendicularly emitted from the heavy axis changes from stable to unstable, keeping self-retracing property. From the maximal Lyapunov exponents  $\lambda_{\max}$ , (a)  $\gamma_{\text{th}} = 0.5723$ , (c)  $\gamma_{\text{th}} = 0.7216$ . A new  $U'$  is born and it is  $NR$ . (See figure 11 for the coexistence of stable and unstable PO). Remarkably period continuously changes through the threshold (see (b),(d)), and, above threshold, periods of  $S(R)$  and  $U'(NR)$  are extremely degenerate despite their distinct orbit profiles.

self-non-retracing respectively. That is, the bifurcation proceed in the process

$$U(R) \rightarrow S(R) + U'(NR), \quad (31)$$

where, R and NR stands for self-retracing and self-non-retracing<sup>14</sup>. See figure 11 for the location of their initial values in the rectangle.

- (2) Below and above threshold,  $\lambda_{\max} \propto |\gamma - \gamma_{\text{th}}|^{1/2}$  gives a good description.
- (3) As discussed in 4.2.2, the initial point  $(X_0^*, U_0^*)$  of the unstable PO ( $U'$ ) above threshold locates at the edge of the overlap of  $F$  and  $P$  ribbons (figure 11).  $U_0^*$  also exhibits the typical threshold behavior  $U_0^* \propto (\gamma - \gamma_{\text{th}})^{1/2}$ .
- (4) It is interesting to note that the period of the periodic orbits are insensitive to the transition. The period of  $U$  as a function of  $\gamma$  below  $\gamma_{\text{th}}$  smoothly continues to that of  $S$  above  $\gamma_{\text{th}}$ . This may be natural since both POs are self-retracing, but the period of the self-non-retracing one ( $U'$ ) is also degenerate in very good approximation.

14 We write R for self-retracing (rather than SR) to avoid confusion with ‘S’ for a stable PO.

### 4.3. Orbit Symmetry Consideration

*4.3.1. Three classes of  $Y$ -symmetric orbits* Since all involved POs in the bifurcation process  $U(R) \rightarrow S(R) + U'(NR)$  are  $Y$ -symmetric, let us now focus on the  $Y$ -symmetric POs. By simple topology and symmetry consideration, we can obtain an overview on this bifurcation process. Firstly, we prepare two keys. (1) A retracing ( $R$ ) PO should be distinguished from a non-retracing ( $NR$ ) PO. A  $NR$ -PO is simply a closed curve and homotopic to  $S^1$ , but, in  $R$ -PO, the particle is going back and forth on the same curve connecting two turning points. To account for this specific feature, let us say  $R$ -PO is homotopic to *squashed*  $S^1$ . See figure 13. (2)  $n_{\perp}$ , the number of perpendicular crossing

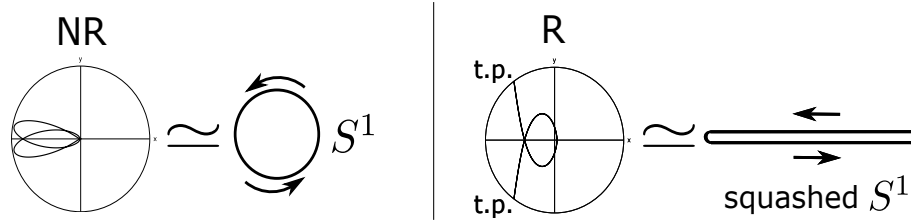


**Figure 13.** A self-non-retracing PO (such as  $U'$  in PO3-6) is homotopic to  $S^1$ , while a self-retracing PO ( $U$  and  $S$ ) is considered to a *squashed*  $S^1$ . In the right, each t.p. denotes a turning point.

of a  $Y$ -symmetric PO with the heavy  $x$ -axis, must be either 2 or 0. This is because an orbit with odd  $n_{\perp}$  cannot be closed while  $n_{\perp} = 4, 6, \dots$  can close but in disconnected loops.

With above preparation, we can prove a remarkable fact:

*Any  $Y$ -symmetric periodic orbit is subject to one of the following three classes;*

- (a) R with  $n_{\perp} = 2$ ,
  - (b) NR with  $n_{\perp} = 0$ ,
  - (c) NR with  $n_{\perp} = 2$ .
- (32)

The key of proof is to consider how to realize with the  $Y$  symmetric orbit an appropriate  $n_{\perp}$  for the topology (retracing or non-retracing). See figure 14(a-c).

- (i) For retracing PO to be  $Y$ -symmetric, at least one perpendicular crossing of the  $x$ -axis must be included. But, being a squashed  $S^1$ , just a single perpendicular crossing already saturates  $n_{\perp} = 2$ . This crossing is multiplicity 2 in itself. Crossings other than it are X-type junction each with multiplicity 4. This is class (a).
- (ii) On the other hand, for a non-retracing PO, it can be  $Y$ -symmetric even without perpendicular crossing; either  $n_{\perp} = 0$  (b) or  $n_{\perp} = 2$  (c).

In (b), all the crossings are X-type junction, each with multiplicity 2.

In (c), all the crossings are X-type but for two distinct perpendicular crossings each with multiplicity one. ■

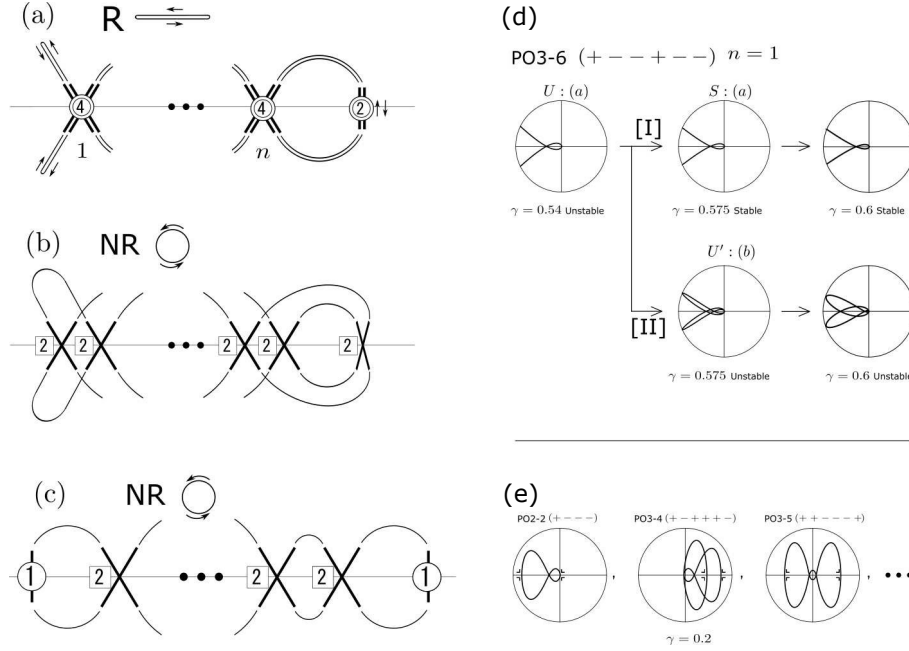


**Figure 14.** (a),(b),(c) Three classes of  $Y$ -symmetric PO. Crossing multiplicities are shown. In (c) two perpendicular crossings (multiplicity one) are set at ends for easy identification. (d) Broucke's PO3-6 bifurcation  $U(R) \rightarrow S(R) + U'(NR)$ .  $U \rightarrow S$  are stability transition within class(a) (route[I]),  $U \rightarrow U'$  is (a)  $\rightarrow$  (b) (route [II]). (e) POs in class (c) ( $\gamma = 0.2$ , all unstable). PO15-1  $S''(NR)$  is also in class (c) (figure 20).

Having proved the classification of  $Y$  symmetric POs, let us reconsider Broucke transition  $U(R) \rightarrow S(R) + U'(NR)$ , and try to understand why the pattern of the bifurcation is in this way in the light of the threshold behavior and the classification theorem in four steps.

- (i)  $S$  must be class (a) (meaning self-retracing): Under the decrease of anisotropy, the orbit is stabilized and  $S$  is born. As found in figure 10, it is just born at the threshold  $\gamma = \gamma_{\text{th}}$ , when the future and past ribbon become tangent each other; hence the location of the initial point  $(X_0^*, U_0^*)$  is in the middle of the maximum ribbon overlap at  $U_0^* = 0$  ( $p_{\perp} = 0$ ). This means perpendicular emission from the heavy  $x$  axis. Hence,  $S$  must be  $Y$  symmetric. Besides, the classification requires that either  $n_{\perp} = 2$  or  $0$ . Since at least there is one perpendicular crossing exists,  $n_{\perp}$  must be  $2$  and the class of  $S$  is either (a) or (c). In (a), the crossing is self-retracing and multiplicity  $2$ , while in (c), two separated perpendicular crossings, each multiplicity one, are necessary. But, as we see in figure 10, at the threshold, there is no room for the separation and (c) is excluded. Therefore,  $S$  should be in class (a), which means  $S$  is self-retracing.
- (ii)  $Y$ -symmetry: The transition  $U \rightarrow S + U'$  is induced by the configuration change of respective F and P ribbons at the threshold, and, as ribbons carry the same code before and after the transition, the PO transition must be code-preserving. As shown by Gutzwiller [4], the code of PO dictates the symmetry of PO, so that

$U$  and  $U'$  must be also  $Y$ -symmetric, once  $S$  is understood to be  $Y$  symmetric. Therefore, we can apply the classification theorem of  $Y$  symmetric PO to all of them.

- (iii)  $U$  is also class (a) (self-retracing):  $Y$ -symmetry of  $U$  is argued above [(2)], but also directly seen in figure 10. It locates at the crossing of the F and P ribbons at  $U_0^* = 0$ , and, just the same reason as [(1)],  $U$  is  $Y$ -symmetric and in class (a). As discussed at figure 10, the  $U(R)/S(R)$  transition here just corresponds to, in term of ribbons, the configuration change single-point/finite-width overlap.
- (iv)  $U'$  is class (b) and non-self-retracing: As  $U$  is now understood to be in class (a), we consider in figure 15 all possible routes, via which the initial  $U(R)$  in class (a) may change its feature through the transition.

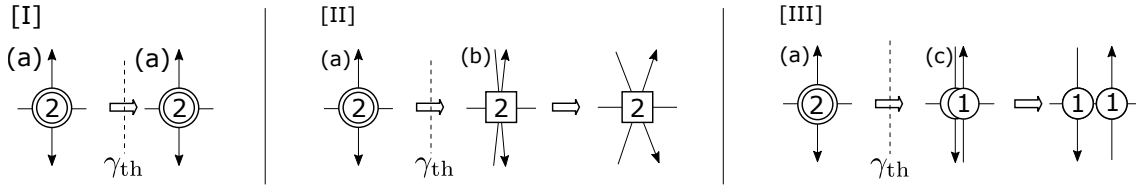


**Figure 15.** Three routes of transition of  $Y$ -symmetric PO with decreasing anisotropy. From class (a) ( $n_{\perp} = 2$ ), [I] it remains in (a) but changes from unstable to stable. [II] ( $a \rightarrow b$ ) ( $n_{\perp} = 2 \rightarrow 0$ ). Non-vanishing  $U_0$  is generated quickly after  $\gamma_{th}$ . [III] ( $a \rightarrow c$ ) No change of  $n_{\perp}$ , but multiplicity at crossing changes as  $2 \rightarrow 1 + 1$ .  $X_0$  changes rapidly after  $\gamma_{th}$ .

Route [I] is ( $a \rightarrow a$ ), but changes from unstable to stable. This is just  $U(R) \rightarrow S(R)$ , and just corresponds to the above single-point/finite-width overlap. The initial value remains  $U_0^* = 0$  and only with small change in  $X_0^*$  occurs. Now, let us discuss the route  $S(R) \rightarrow U'$ . ( $U'$  must be  $Y$  symmetric, as the transition is code-preserving). It can be in principle either via [II] or [III]. In [II], the self-retracing property is broken, and the  $n_{perp} = 2$  crossing becomes  $X$ -crossing. Then, non-vanishing  $U_0$  is generated quickly after  $\gamma_{th}$ . This is just in accord with the threshold behavior of  $U'$  ( $U_0^* \propto (\gamma - \gamma_{th})^{1/2}$ ); unstable with initial value at the edge of the overlap of F and P ribbons. (On the other-hand, if the route were via [III], retracing-property is broken in such a way that rapid  $\Delta X_0$  is created without  $\Delta U_0$ . This is totally against the threshold behavior of ribbons). Thus, the route must be via [II] and  $U'$  must be  $U'(NR)$

The above is a *a post-diction* on the Broucke' transition and summarized in figure 14(d). It is just the transition as it is. Two remarks are in order;

- (1) For a PO in class (a), the total number of crossings of the  $x$ -axis (i.e. the length) is  $4n + 2$ ,  $4n$  comes from  $n$  cross-junction with multiplicity 4 and 2 from a single perpendicular crossing with multiplicity 2. The rank of a PO is half of its length; thus, the rank of class (a) PO must be odd ( $2n + 1$ ). For this reason, we conjecture

that the Broucke-type transition, associated with the non-shrinking ribbon, will occur in  $Y$  symmetric odd rank PO.<sup>15</sup>

- (2) We have observed route III transition for a PO in rank 15, where  $\gamma > 9/8$ . See figure 18 below.

## 5. Application

### 5.1. The two-dimensional AKP PO search

In order to study the POs in this system, especially to challenge the uniqueness issue, we first of all have to search out the POs *exhaustively*. By exhaustively we mean avoiding any limitation on the PO, irrespective of its symmetry and whether it is unstable or stable. The recent search by Contopoulos et al. [20] was of this type but it is limited to perpendicular emission from the heavy axis ( $p_{0,y} = 0$ ). Then, choosing the initial position  $x_0$  on the heavy axis ( $y_0 = 0$ ) also fixes the momentum  $p_{0,x}$  via energy conservation; hence a one-parameter shooting varying  $x_0$  only is sufficient. Their analysis yielded important information especially on the existence of stable PO in AKP including relatively high rank PO. However, the limitation is rather severe; it limits the PO only to the  $Y$ -symmetric ones. Furthermore, it cannot detect the class (b),  $n_{\perp} = 0$ , PO ( $NR$ ) which is created as  $U'(NR)$  after the bifurcation  $U(R) \rightarrow S(R) + U'(NR)$ . To be exhaustive, we organize our search as follows.

- (1) The basic flow of the analysis is based on specifying the code of a PO at a certain anisotropy. For instance, if the code (+ - - + --) is specified, the routine searches out Broucke' PO-36;  $U(R)$  only if  $\gamma < \gamma_{th}$ , but both  $S(R)$  and  $U'(NR)$  if  $\gamma > \gamma_{th}$ . One can be sure that there is no more PO of this code within the setup resolution. Figure 10 and 11(a-c) are the outcome of the code request (+ - - + --).
- (2) Given the requested code of PO, we now take advantage of the PO trapping mechanism. That is, the properness of the tiling of  $D_0$  by ribbons guarantees that  $(X_0^*, U_0^*)$  should be inside the base ribbon of the step whose height  $\zeta_N^F(a)$  is calculated by (9). We use  $N = 48$  for the maximum precision in the double precision calculation.
- (3) The above *asymptotic* ribbon with  $N = 48$  may be, if it subjects to case (A), extremely narrow ( $\Delta X \sim O(1/2^{48})$ ) and the neighboring steps may be almost degenerate in heights. On the other hand, if it is in case (B), it may retain some finite width. Here we proceed protectively; rather than directly tackling the asymptotic ribbon, we focus on level  $2n$  ( $\ll 48$ ) ribbon, which should embody

<sup>15</sup> Precisely, the tangency of the F and P ribbons at  $U_0 = 0$  implies  $Y$ -symmetry of involved POs, and  $n_{\perp} = 2$ , but the possibility of the pre-PO ( $U$  in the Broucke's case) being in class (c) is not logically excluded. Our preliminary result is that from  $n = 3$  up to  $n = 23$  and  $\gamma < 8/9$ , there is only one advent of non-shrinking ribbons at every odd rank starting from (a). We are trying to consolidate this issue.



the asymptotic one by the properness of the tiling<sup>16</sup>. The interval of the ribbon,  $(X_0^{\min}, X_0^{\max})$  at the mesh points of  $U_0 \in (-B, B)$  can be calculated by a bi-section method to satisfy

$$\zeta_{2n}^F(X_0^{\min}, U_0) \leq \zeta_N^F(a) \leq \zeta_{2n}^F(X_0^{\max}, U_0) \quad (33)$$

Now the search area is reduced from vast  $D_0$  to a level  $2n$  ribbon extending from  $U = -B$  to  $U = B$ .

- (3a) At this step, we check whether the target ribbon shrinks or not by inspection of its full profile  $U_0 \in (-B, B)$ .
- (4) Now the shooting for a PO inside the level  $2n$  ribbon— find a point that makes the misfit

$$\chi^2(X_0, U_0) \equiv (x_F - x_0)^2 + y_F^2 + (p_{x,F} - p_{x,0})^2 + (p_{y,F} - p_{y,0})^2 \quad (34)$$

between the initial and final  $2n$ -th crossing of the  $x$ -axis vanishing<sup>17</sup>. Practically we have firstly searched for  $X_0^*$ , which minimizes  $\chi^2$ , at every  $U_0$ . This gives a function  $X_0^*(U_0)$  over the interval  $(-B, B)$ , and through it, we can regard  $\chi^2$  as a function of  $U_0$ . That is,

$$\chi^2(U_0) \equiv \chi^2(X_0^*(U_0), U_0).$$

Thus, the two-parameter search is effectively reduced to one-parameter one.

- (4a) In case (A),  $\chi^2(U_0)$  should be a convex function of  $U_0$  with a single bottom at  $U_0^*$  with vanishing  $\chi^2$  within numerical error. Then  $(X_0^*, U_0^*)$  is the wanted for initial position<sup>18</sup>. In case (B),  $\chi^2(U_0)$  turns out multi-bottomed vanishing at each bottom. To deal with both possibilities, graphical analysis of the full profile of  $\chi^2(U_0)$  is performed.
- (5) We combine the information from the past ribbon on top of the above procedure.

With step (3a) and (4a), the search is organized not to miss the violation of uniqueness. Below, we report two applications; a detailed case study of a high-rank PO ( $\gamma = 0.85 - 0.93$ ) and an exhaustive PO search regarding the uniqueness issue at high anisotropy ( $\gamma = 0.2$ ).

## 5.2. The case study of bifurcations of a high-rank PO ( $n = 15$ ).

The investigation of this PO is motivated by the longest PO (length 30) among the stable POs reported by Contopoulos et al. [20]. However, the code of their PO is not given and there is a possibility of miss-identification, considering the exponentially large

<sup>16</sup> This corresponds to the relaxed ribbon with boundaries  $\mathcal{B}_L$  and  $\mathcal{B}_R$  in figure E1.

<sup>17</sup>  $y_F \equiv 0$  by definition.  $(X_0, U_0)$  in the left-hand side fixes the initial point in the Cartesian coordinates, and the integration of orbit for the calculation of right-hand side is done in  $x, y, p_x, p_y$ , with slow down around the origin when close-encounter with the origin is involved.

<sup>18</sup> In this case, bottom-search by a tri-section method on  $\chi^2(U_0)$  is vital. See our earlier report [21].

number of POs at such high rank. Thus, the description below may be better read in its own right irrespective to the motivation<sup>19</sup>. The code of our PO15 is

$$(+ - + - + - + - - + - + - + -)^2. \quad (35)$$

We find it bifurcates twice;  $U \rightarrow S + U'$  and then  $S \rightarrow S' + S''$  as seen in figure 16. The bifurcation pattern is summarized in figure 17 using the PO class (figure 14) and bifurcation route (figure 15). As the orbit at this high rank is very complicated, let us examine the bifurcation as a challenge to the general theory consideration in section 4.

(1) The first bifurcation  $U \rightarrow S + U'$ : All  $U, S, U'$  are  $Y$ -symmetric and our

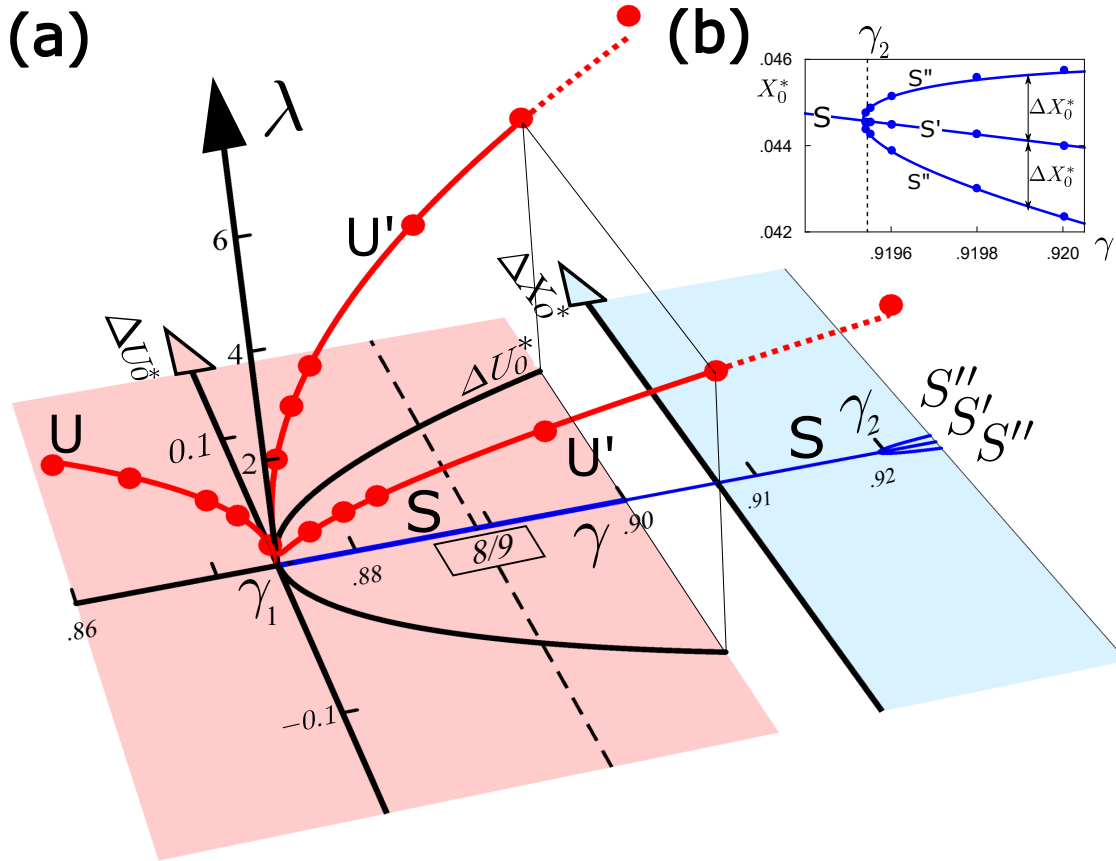


**Figure 16.** (a) A rank 15 PO bifurcates twice;  $U(R) \rightarrow S(R) + U'(NR)$  and then  $S(R) \rightarrow S'(R) + S''(NR)$ . The coordinates are  $(\Delta U_0^*, \gamma, \lambda)$  and  $(\Delta X_0^*, \gamma, \lambda)$  respectively. Curves are from a simple fit  $\lambda_{\max} = a\theta(\gamma_1 - \gamma)\sqrt{\gamma_1 - \gamma} + b\theta(\gamma - \gamma_1)\sqrt{\gamma - \gamma_1}$ ,  $(\gamma_1, a, b) = (0.8743, 22.36, 30.87)$  and  $U_0^* = \pm c\sqrt{\gamma - \gamma_{1,U}}$ ,  $(\gamma_{1,U}, c) = (0.8744, 0.6822)$  give good fit with  $|\gamma_1 - \gamma_{1,U}| \leq O(10^{-4})$ . (b) magnifies the stable PO's bifurcation near the threshold. The fit is  $\Delta X_0 = c\sqrt{\gamma - \gamma_2}$ ,  $(\gamma_2, c) = (0.9195, 0.07818)$ .

classification can be applied. Figure 16 shows that the initial value of  $U, S$  is  $U_0^*$ , while

<sup>19</sup> We read  $x_0$  by eye from their Figs.4 and 6, and confirmed reproduced orbit closes, below bifurcation threshold, at the stated 30-th crossing after slight adjustment. But, passing the threshold, it gradually fails to close. Their analysis is limited to  $p_{x,0} = 0$ , and there is a possibility of error, that observed PO is the same with ours ( $U(R) \rightarrow U'(NR) + S(R)$ ), where  $U'(NR)$  is  $p_{x,0} \neq 0$ . We here quote our initial values  $(X_0, U_0)$  with sufficient digits for reproduction. At  $\gamma = 0.87$ , there is only  $U$ :(0.11465, 0), and at  $\gamma = 0.88$ , there are both  $S$ :(0.099342, 0) and  $U'$ : (0.10021, 0.050793).

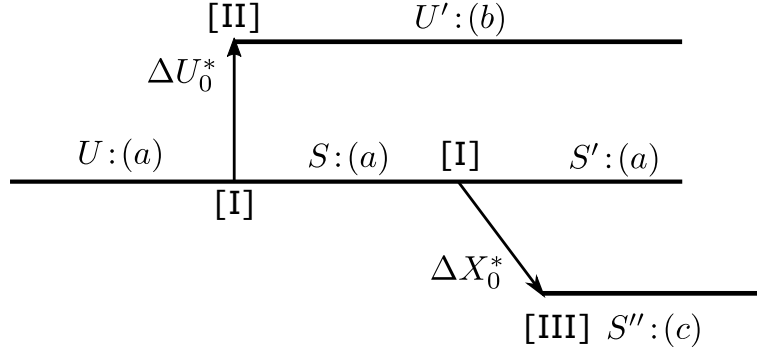


**Figure 17.** Bifurcation scheme of the PO15.

the  $U_0^*$  of  $U'$  is rapidly created after the bifurcation. This leads us to infer  $U \rightarrow S$  is via route [I] ( $(a) \rightarrow (a)$ ) and  $U \rightarrow U'$  is via route [II] ( $(a) \rightarrow (b)$ ). This means the bifurcation is  $U(R) \rightarrow S(R) + U'(NR)$ ; just the same with Broucke's PO3-6 and PO5-40. The ribbon structure in figure 18 consistently shows that the bifurcation is exactly caused along with the advent of non-shrinking ribbon.  $(X_0^*, U_0^*)$  of  $U'$  locates at the edge of the overlap, while that of  $S$  is at the center of the overlap with  $U_0^* = 0$ . Now,

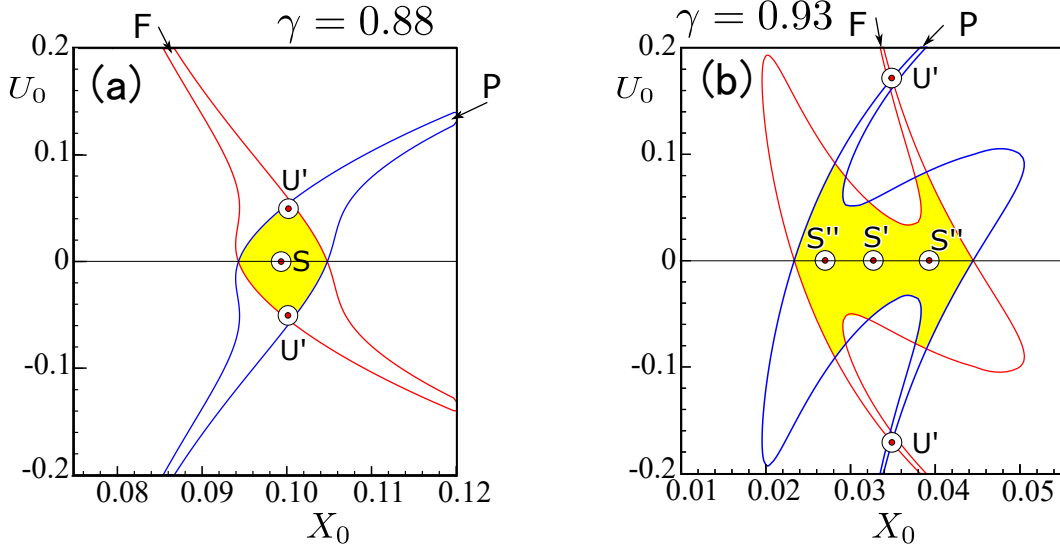


**Figure 18.** Initial points of a PO15 (a) after  $U \rightarrow S + U'$ , (b) after  $S \rightarrow S' + S''$ .

the orbit profiles are given in figure 19. As orbits are length 30, they look at a glance as a cloud but from the density, apparently  $S$  is self-retracing and  $U'$  is non-retracing. One can also pin-point the tuning-point at the kinematically boundary in the latter. The close inspection is more intriguing;  $S(R)$  has a single  $n_2$  point, while  $U'(NR)$  has two perpendicular crossings, each with multiplicity one. This is just the multiplicity prediction from the classification (32) and figure 15.

The second bifurcation  $S \rightarrow S' + S''$ : This is a new case, which occurs in the very low anisotropy regime ( $\gamma_2 > 8/9$ ), where the flow (A.3) has no longer hyperbolic singularities and the existence of unstable PO at an arbitrary code is no longer guaranteed [16].

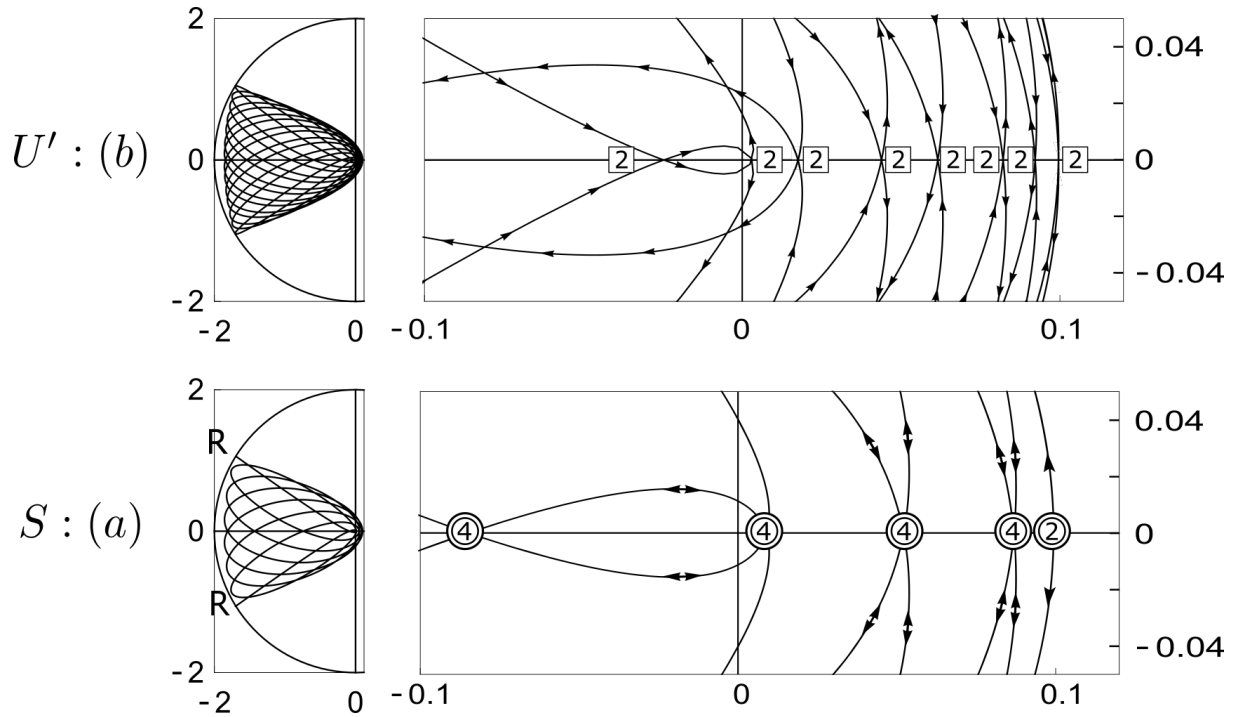


**Figure 19.** A rank 15 PO.  $\gamma = 0.88$ . Crossing multiplicity shows  $U'(NR)$  ( $S(R)$ ) is class (b) [(a)].

The rapid initial value variation is in the  $X$  direction. Thus, we infer that  $S''$  is produced via root [III], which means it is in class (c) and the bifurcation should be  $S(R) \rightarrow S'(R) + S''(NR)$ . Indeed, the initial positions of  $S'$  and  $S''$  in figure 18 are horizontally aligned. Horizontal because the variation is in the  $X_0$  direction, and two initial points for  $S''$  because  $S''$  is in class (c) ( $n_{\perp} = 2$ ). (See the two multiplicity-one crossings in [III] in figure 15). This can be directly verified in the orbit profile in figure 20(c). Let us note a further success of the theory. It tells  $U'$  must be  $NR$  but it can be hardly seen from the orbit since the orbit is almost doubled and looks as though self-retracing. However, the twice magnification in figure 20(a) verifies it is indeed  $NR$ .

Summing up, the PO15 first bifurcation follows precisely the theory classification, and the theory also explains the second bifurcation which embodies class (c) PO.

### 5.3. Search of all distinct POs (rank $n \leq 10$ ) at high anisotropy $\gamma = 0.2$

Here we report our exhaustive search for the POs up to rank  $n = 10$  (length  $2n = 20$ ) at the high anisotropy ( $\gamma = 0.2$ ). As noted in the introduction, it was previously considered that at such high anisotropy all POs are unstable and isolated, mainly based on the early numerical analysis [4, 7]. On the other hand, recently some possibility has been expressed in [20] that the existence of ample stable orbits in AKP may indicate stable orbits even at high anisotropy. Therefore, we here revisit high anisotropy AKP armed by our two-parameter shooting algorithm which embodies steps (3a) and (4a) above so that it is sensitive to the possible violation of uniqueness.



the degeneracy is halved for each self-symmetry<sup>20</sup>. There are ten symmetry types of PO, five for a non-self-retracing (NR) and five for a self-retracing (R) PO. The degeneracy factor for each symmetry-type is listed at the fourth row of table 2. The  $O$  type among

**Table 2.** The number of distinct POs predicted under uniqueness assumption in each of ten symmetry classes indexed by  $k$ . The fourth row lists the degeneracy  $\sigma_{\text{sym}}(k)$ .

	Non-self retracing: NR					Self-retracing: R					
	—	$X$	$Y$	$XY$	$O$	—	$X$	$Y$	$XY$	$O$	
Sym.Type $k$ :	1	2	3	4	5	6	7	8	9	10	
$\sigma_{\text{sym}}(k)$ :	8	4	4	2	4	4	2	2	1	2	
Rank $n$											total #
1	0	0	0	1	0	0	0	1	0	0	2
2	0	0	1	1	0	0	1	1	0	0	4
3	0	1	2	2	0	1	0	2	0	0	8
4	2	2	7	1	0	2	3	1	0	0	18
5	12	6	12	4	0	6	0	4	0	0	44
6	57	14	30	2	0	13	4	2	0	0	122
7	232	28	57	8	1	28	0	8	0	0	362
8	902	62	127	1	0	58	11	1	0	0	1162
9	3388	120	247	16	7	120	0	16	0	0	3914
10	12606	264	508	4	0	246	16	4	0	0	13648

$NR$  is newly found at rank 7 and 9, see discussion below. The number of distinct POs in a given symmetry class listed in the following rows are predicted (under the uniqueness assumption) by counting *distinct* sequences. The prescription is given by Gutzwiller in detail and the code table up to rank  $n = 5$  is given in Table I of [4]. Our table 2 is its extension to  $n = 10$ . (Explicit sequences take pages and only the number of sequences is tabulated). Now, let us briefly recapitulate the prescription. First, a rank  $n$  PO is represented by a length  $2n$  binary code; if the orbit traverses the heavy axis upwards  $n$  times, then it must traverse also  $n$  times downwards to come back the initial point. Next, the symmetry of a PO corresponds to the rule of its code. For instance, if a PO is  $X$  symmetric, its code must satisfy a rule  $X : a_{2n-i-1} = -a_i$  [4]. Thus, as all POs are divided into classes by the equivalence under symmetry transformation in order to scrutinize distinct POs, the  $2^{2n}$  binary sequences at rank  $n$  should be divided into classes using symmetry rules. However, to reach distinct sequences, it is not sufficient to divide by the equivalence under  $X, Y, \mathcal{T}$  rules, but one must also divide by the equivalence of sequences under the code-shift operation  $\tau$ , that is, the freedom of choosing the starting bit among the cyclic binary code. At this final step, there is a slight subtlety. If the rank  $n$  is prime, the code-shift symmetry simply amounts to  $n$ -fold degeneracy. (It is  $n$

<sup>20</sup> If a PO is non-self-retracing,  $\mathcal{T}$  produces degenerate pairs orbiting in opposite-direction each other, but if self-retracing,  $\mathcal{T}$  is immaterial—after it amounts to simply the freedom of the choice of one among two turning points as the starting point.

rather than  $2n$ , because, by definition, the starting bit must be chosen from crossings with  $p_y > 0$ ). However, it must be noted that the set of rank  $n$  POs includes  $m$  times repetition of a lower rank primary orbit of rank  $p$ , where  $p$  a prime divisor  $p = n/m$ . In such a case, the code-shift degeneracy reduces to  $p$ . Dividing out the code-shift degeneracy taking account this, one eventually reaches the distinct sequences. Table 3

**Table 3.** The number of distinct codes  $N(p, k)$  is tabulated as a  $p$ -th row,  $k$ -th column element, where  $p|n$  counts the code-shift degeneracy and  $k$  labels symmetry class (see table 2) with  $\sigma_{\text{sym}}(k)$  in the square bracket. Rank  $n = 9$  (upper) and 10 (lower). This is obtained by dividing codes by orbit symmetry and by code-shift equivalence, thus  $\sum_{p|n} \sum_k p N(p, k) \sigma_{\text{sym}}(k) = 2^{2n}$ . The bottom row,  $\sum_{p|n} N(p, k)$  gives number of distinct codes in each symmetry class.

$N(p, k)$	1[8]	2[4]	3[4]	4[2]	5[4]	6[4]	7[2]	8[2]	9[1]	10[2]	#codes <sup>a</sup>
9	3388	119	245	14	7	119	0	14	0	0	262080
3	0	1	2	1	0	1	0	1	0	0	60
1	0	0	0	1	0	0	0	1	0	0	4
3914	3388	120	247	16	7	120	0	16	0	0	$2^{18}$

$N(p, k)$	1[8]	2[4]	3[4]	4[2]	5[4]	6[4]	7[2]	8[2]	9[1]	10[2]	#codes <sup>a</sup>
10	12594	258	495	0	0	240	15	0	0	0	1047540
5	12	6	12	3	0	6	0	3	0	0	1020
2	0	0	1	0	0	0	1	0	0	0	12
1	0	0	0	1	0	0	0	1	0	0	4
13648	12606	264	508	4	0	246	16	4	0	0	$2^{20}$

<sup>a</sup>  $\sum_k p N(p, k) \sigma_{\text{sym}}(k)$ .

shows how to organize this counting. Uniqueness of a PO for a given code means one and only one distinct PO for each distinct code. Under this assumption, the bottom row of table 3 gives the number of distinct PO prediction in table 2.

*5.3.2. The results: uniqueness holds at  $\gamma = 0.2$*  Now, we describe how the checker (3a) and (4a) in the algorithm worked.

- (3a) Always the ribbon of the code shrinks at  $\gamma = 0.2$  as  $\sim 1/2^{2n}$ . Specifically for  $n = 10$ , the maximum width,  $\max(X_0^{\max}(U_0) - X_0^{\min}(U_0))$  (see (33)) over the interval  $U_0 \in (-B, B)$  does not exceeds  $10^{-7}$  for any one of the tested 13648 codes. (See table 2)
- (4a) Always the chi-squared (misfit) curve is convex with a single bottom with negligible value. It is mostly under  $10^{-20}$  (the best value is  $\sim 10^{-25}$ ) and the worst is  $\sim 10^{-2}$  only for a few POs.
- (5) The bottom  $(X_0^*, U_0^*)$  agrees without exception with the crossing point of the future and past *lines*. (At large  $N$  ribbons are reduced to lines in the scrutiny at  $\gamma = 0.2$ ).

Subsequent stability test has proved that all the PO are unstable. Therefore, we conclude that within the above resolution, there are only unstable POs and that the PO is unique for any given code up to  $n = 10$  at  $\gamma = 0.2$ .

*5.3.3. A new symmetry type O and other PO samples* Let us comment on the new symmetry class (*O* type). This type is not considered in Gutzwiller [4]. We are firstly embarrassed when we cannot satisfy by the search result the sum rule that number of the PO should be  $2^{2n}$  when division by the symmetry equivalence is removed. It may have indicated the violation of uniqueness even though we are working at the highly chaotic region  $\gamma = 0.2$ . Eventually we were able to locate the reason as due to this *O*-type; there is only one at rank  $n = 7$  and seven at rank 9. After counting correctly them, the sum rule is satisfied, and the uniqueness holds at  $\gamma = 0.2$ . See table 2. The *O* type orbit is neither *X*– nor *Y*–symmetric, but symmetric under the transformation  $O : x \rightarrow -x, y \rightarrow -y$ . The observed ones are all self-non-retracing and ( $\sigma_{\text{sym}} = 2^2$ ). The symmetry class number 5 is assigned, 10 is reserved for the possible occurrence of *O*-type retracing PO at  $n \geq 11$ .

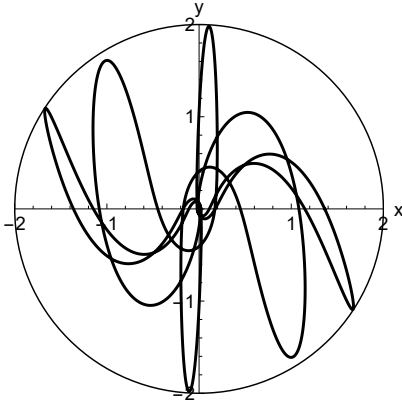


**Figure 21.** *O* symmetric orbit at rank  $n = 9$ .

$(n, \text{Id})$	(9, 2285)								
symmetry	$A_X A_Y$ but <i>O</i>								
$X_0$	1.6938906682974								
$U_0$	-0.6845071038062								
$\lambda_{\text{max}}$	14.73								
Action	40.05								
code	0	1	2	3	4	5	6	7	8
	+	+	-	+	+	-	+	-	-
	9	10	11	12	13	14	15	16	17
	-	-	+	-	-	+	-	+	+

Further examples are taken from 13648 distinct unstable POs at rank 10. The last one is *Y*-symmetric and *NR*, then our classification tells it is in class (c). Indeed close investigation reveals it has two perpendicular crossings, each multiplicity one as the class (c) PO should.

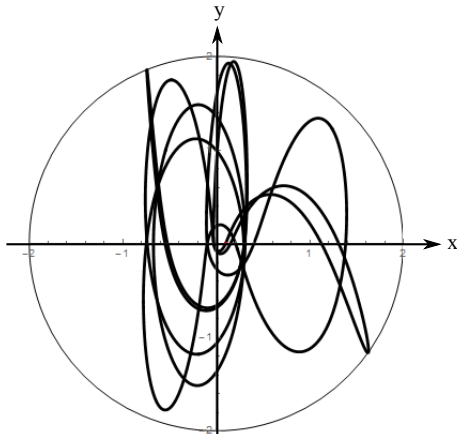
#### 5.4. A Verification of the Gutzwiller's Action Formula

In Gutzwiller's periodic orbit theory, the semi-classical description of the quantum density of state is given by

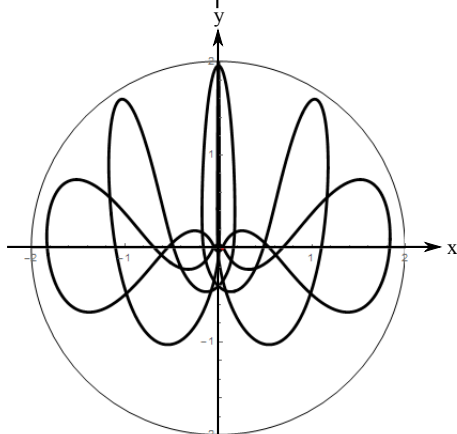
$$g(E) \equiv \sum_i \frac{1}{E - E_i + i\epsilon} \approx g_{\text{POT}}(E) \equiv -\frac{i}{\hbar} \sum_{\Gamma \in \text{POs}} \frac{T_{\Gamma,0}}{2 \sinh(\lambda_{\Gamma}/2)} e^{iS_{\Gamma}(E)/\hbar - i\pi\nu_{\Gamma}/2}, \quad (36)$$

where the sum is over all classical periodic orbits. Each PO is designated by  $\Gamma$ ;  $S_{\Gamma}$ ,  $\lambda_{\Gamma}$ ,  $\nu_{\Gamma}$  are respectively action, Lyapunov exponent, and number of conjugate points of  $\Gamma$ ,

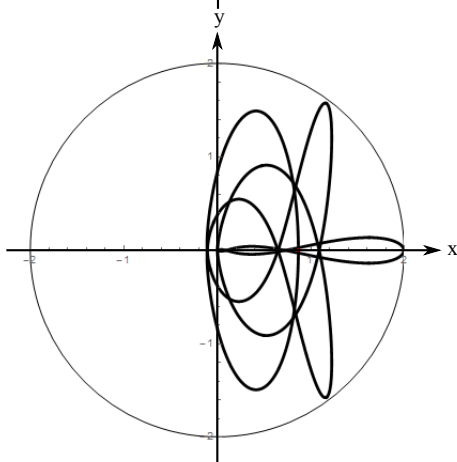




$(n, \text{Id})$	(10, 10000)									
symmetry	$A_X, A_Y$ ( $k=1$ )									
$X_0$	1.073770101110692									
$U_0$	0.806561621655999									
$\lambda_{\max}$	14.31908020947697									
Action	49.36092248823712									
code	0	1	2	3	4	5	6	7	8	9
	+	+	+	+	-	+	-	-	+	-
	10	11	12	13	14	15	16	17	18	19
	+	+	+	-	-	+	-	+	-	-



$(n, \text{Id})$	(10, 5002)									
symmetry	$S_X, A_Y$ ( $k=2$ )									
$X_0$	1.200325396087828									
$U_0$	0.8860249568347829									
$\lambda_{\max}$	17.46793360630122									
Action	40.77425334607968									
binary code	0	1	2	3	4	5	6	7	8	9
	+	+	+	+	+	-	+	+	-	+
	10	11	12	13	14	15	16	17	18	19
	-	-	+	-	-	-	-	-	+	-



$(n, \text{Id})$	(10, 100)									
symmetry	$A_X, S_Y$ ( $k=3$ )									
$X_0$	0.8662601476594602									
$U_0$	0.									
$\lambda_{\max}$	19.36441255533023									
Action	30.64876862775776									
binary code	0	1	2	3	4	5	6	7	8	9
	+	-	+	+	-	+	+	+	+	+
	10	11	12	13	14	15	16	17	18	19
	+	+	+	+	+	+	-	+	+	-

**Figure 22.** Sample orbits at rank 10. The first is asymmetric under both  $X$  and  $Y$ ;  $k = 1$  in the notation of table 2. The third is  $Y$  symmetric; class (c) because  $NR$ .

while  $T_{\Gamma,0}$  is the period of the primary cycle of  $\Gamma$ . From the scaling property of AKP, the action behaves as  $S_{\Gamma} = \Phi_{\Gamma}/\sqrt{-2E}$  with a constant  $\Phi_{\Gamma}$  characteristic to each PO. In the endeavor to calculate  $g_{POT}(E)$  in (36), Gutzwiller first introduced the symbolic coding of the PO in order to put the sum under control. The next step was to express the

constant  $\Phi_\Gamma$  by the binary code of the PO.<sup>21</sup> For this issue he introduced the following empirical formula for  $\Phi(a)$  of a periodic orbits of rank  $n$  (length  $2n$ ) with the primary code  $a = (a_0, a_1, \dots, a_{2n-1})$

$$\Phi(a) = 2n\tau \cosh\left(\frac{\lambda_A}{2}\right) - \frac{1}{2}\tau \sinh \lambda_A \sum_{i=1}^{2n} \sum_{j=-\infty}^{+\infty} a_i a_j e^{-\lambda_A |j-i|}. \quad (37)$$

This formula has only two parameters,  $\tau$  and  $\lambda_A$ , but it was found that, for  $n = 5$ , this formula can provide  $\Phi$  of any PO in remarkable agreement with the measured value.<sup>22</sup> We have performed the test of this formula using the action of rank  $n = 10$  PO obtained by our high accuracy measurement. In one of the tests, we first determined the two parameters by fit to the action data of 44 distinct POs in the rank  $n = 5$  family. ( $\gamma = 0.2$  [ $\mu^2 = 5$ ]). The result is

$$\begin{aligned} \tau &= 2.871 \quad (2.8844) \\ \lambda_A &= 0.6014 \quad (0.622) \end{aligned} \quad (38)$$

Quoted figures in the parenthesis are from [3] for the Silicon anisotropy ( $\mu^2 = 4.80$ ). Now, we test whether this formula with the parameters fixed at the values in (38) can endure the extrapolation to  $n = 10$  family. In figure 23 we show the result as a scatter plot. At  $n = 10$  there are 13648 distinct POs. Each point in the plot represents one of

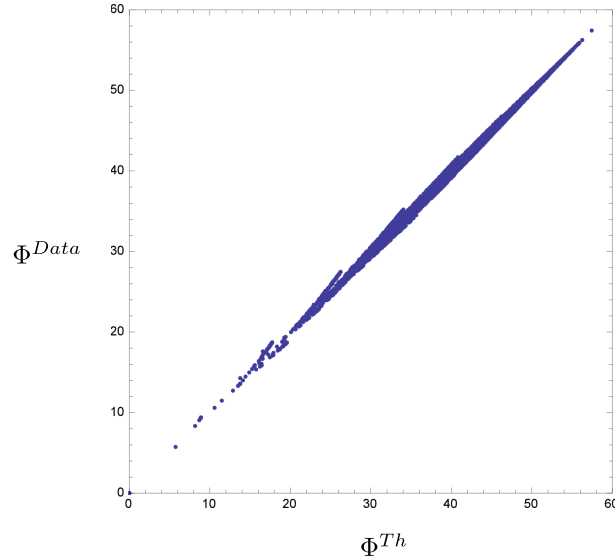


**Figure 23.** The scatter plot of  $(\Phi_{Id}^{Th}, \Phi_{Id}^{Data})$ . *Id* labels each of the distinct 13648 POs in the  $n = 10$  family.

them. it can be seen that the prediction works for the wide range of the action constant

<sup>21</sup>  $T(E) = \frac{\partial S}{\partial E} = S/(-2E)$  and for our canonical choice  $E = -1/2$ ,  $T=S$ , and  $T_{\Gamma,0}$  was obtained by dividing it by  $n$ . For Lyapunov exponent, a ‘crudest approximation’  $\lambda = n\lambda_0 \sim 1.5n$  was adopted in [3].

<sup>22</sup> For the family of rank  $n$  PO, the  $\Phi_{\max}$ ,  $\Phi_{\min}$  and  $\langle \Phi \rangle$  predicted by (37) are easily calculated as  $\Phi_{\min} = 0$ , and (at large  $n$ )  $\Phi_{\max} = 2n\tau$ ,  $\langle \Phi \rangle = 2n\tau(1 + e^{-\lambda_A})$ .

value extending up to 50. We show in table 4 the MSD defined as

$$\text{MSD} = \frac{\sum_{i \in \text{rankndistinctPOs}} (S_i^{\text{Data}} - S_i^{\text{Th.}})^2}{\text{numberofdistinctPOs}}. \quad (39)$$

**Table 4.** The MSD. The formula (37) (with parameter  $\tau$  and  $\lambda$  fixed at level  $n = 5$ ) can describe all  $n$  up to 10 almost with equal accuracy at  $n = 5$ .

rank n	1	2	3	4	5	6	7	8	9	10
# PO	2	4	8	18	44	122	362	1162	3914	13648
MSD	0	0.00965	0.0229	0.0379	0.0500	0.0521	0.0499	0.0494	0.0506	0.0536

As clearly seen the marvelous success of the formula (37) continues up to  $n = 10$ .

Let us briefly discuss the implication of this success. Following Gutzwiller, let us integrate the density of state up to  $E$  [3]. Then, we obtain

$$\int^E dE' D_{\text{POT}}(E') = \sum_n \sum_a \frac{1}{2n \sinh(\lambda_\Gamma/2)} e^{-s\Phi(a)}, \quad (40)$$

where  $a$  is the code of the PO, and a dimensionless variable  $s$  is introduced by

$$s\Phi = -iS/\hbar. \quad (41)$$

By this ‘Wick rotation’, the quantum formula is mapped to statistical formula — the grand partition function of a statistical spin system.<sup>23</sup> Under this transformation, the action formula (37) corresponds to an Ising spin chain, which has only two body interaction with exponential decay. Now that the validity of (37) has been confirmed even up to  $n = 10$ , it may be stated that AKP semi-classical quantum theory at the high anisotropy region is dual to the above spin theory.

## 6. Conclusion

In this paper, we have fully used the ability of symbolic coding in AKP and considered level  $N$  devil's staircase surface and the tiling of the initial value domain by ribbons introduced by the surface. We have proved the properness of the tiling by ribbons from the creation mechanism of  $N + 1$  from  $N$  tiling, which clarifies how the non-shrinking ribbon can emerge.

Our key points are as follows;

- (i) Non-shrinking ribbon emerges when future and past asymptotic curve becomes tangent each other at  $U_0 = 0$  at threshold anisotropy.

<sup>23</sup> Under an approximation  $2 \sinh(\lambda_\Gamma/2) \approx \exp(\lambda_\Gamma/2)$ , the Lyapunov exponent can be traded to a chemical potential.

- (ii) The bifurcation is  $U(R) \rightarrow S(R) + U'(NR)$ . Initial point  $(X_0^*, U_0^*)$  of stable PO  $S$  locates in the overlap of future and past ribbons, while the unstable PO  $U'$  locates at the edge of the overlap.
- (iii) From topology and symmetry consideration, we have explained the above bifurcation scheme, and we give a conjecture that the stable PO occurs in the  $Y$ -symmetric rank odd self-retracing orbit. A case study of high-rank PO15 supports it.
- (iv) An exhaustive PO search verifies the uniqueness conjecture holds at high anisotropy  $\gamma = 0.2$  (if newly found type  $O$  orbit is accounted for). The Gutzwiller's action approximation formula works amazingly for all POs up to rank 10 at this anisotropy.

The topology and symmetry approach developed in this paper gives a frame to constrain the bifurcation, but, we admit that a direct analytical understanding of the advent of non-shrinking ribbon is most wanted for. Relatedly, it is tempting to look at this bifurcation from quantum side—separating of  $S$  and  $U'$  from quantum data, using inverse chaology as *a quantum prism*. Previously, we could successfully extract low rank unstable PO data (including Lyapunov exponents) from AKP quantum spectrum [12]. To tackle with the bifurcation is a serious challenge; it requires higher order correction in  $\hbar$  as well as taking satellite POs into account [23–25]. Work in this direction is in progress.

## Acknowledgments

This paper is an outcome of a course of several years' work in AKP; both KK and KS wrote their Ph. D. theses on their contribution. Taking this occasion, we would like to thank people who gave us useful suggestions and encouragement at various stages of the work. We thank our colleagues, S. Ishihara for useful discussion, T. Nakajima for his enthusiasm in the search of non-shrinking ribbons at the later stage, E. N. Bjerrum-Bohr, P. Damgaard, W. Ochs for unfailing encouragement. We thank people working on dynamical systems, especially M. Saito, M. Shibayama, and K. Tanikawa for their interest and various suggestions. Finally, we would like to thank M. Gutzwiller for his kind correspondence in 2008 (just once). We have send him one of our papers at early stage, and after answering our questions, he wrote that [he is] “a great admirer of figures . . .”, and kindly guided us to [4], encouraging to publish our results. We regret that we can no longer send this completed paper to him and ask for his criticism. This work is partially supported by Research Project Grant (B) by Institute of Science and Technology, Meiji University.

## Appendix A. The Boundary One-time Map $\mathcal{F}_I$

In terms of double polar coordinates (12) the equation of motion given by the Hamiltonian (1) is

$$\frac{d\chi}{dt} = -\frac{(1+e^{2\chi})^2}{4e^\chi} (\sqrt{\nu} \cos \vartheta \cos \psi + \sqrt{\mu} \sin \vartheta \sin \psi), \quad (\text{A.1})$$

$$\frac{d\vartheta}{dt} = -\frac{(1+e^{2\chi})^2}{4e^\chi} (\sqrt{\mu} \cos \vartheta \sin \psi - \sqrt{\nu} \sin \vartheta \cos \psi), \quad (\text{A.2})$$

$$\frac{d\psi}{dt} = -\frac{1}{2}e^\chi (1+e^{2\chi}) (\sqrt{\nu} \cos \vartheta \sin \psi - \sqrt{\mu} \sin \vartheta \cos \psi). \quad (\text{A.3})$$

We consider the limit  $\chi \rightarrow \infty$ ; this corresponds to  $r \rightarrow 0$ , because  $r = 2/(1+e^{2\chi})$  under the choice  $H = -1/2$ . We also slow down the trajectory by a transformation of the time variable  $dt' = e^{3\chi}dt$  to remove the singularity. Then the first two equations become autonomous form (14) and the  $\chi$ -equation decouples (in fact  $\chi$  remains  $\infty$  for any finite  $t'$ ), and (14) describes the evolution of  $\vartheta$  and  $\psi$  in the limit  $\chi \rightarrow \infty$  [2].

The one-time map,  $\mathcal{F}$  in (11), describes how  $D_0$  is mapped onto  $D_1$ . Because the limit  $\chi \rightarrow \infty$  restricts  $D$  to the collision manifold  $I$  (5), (14) embodies all necessary information to find restricted one-time map  $\mathcal{F}|_I : I \rightarrow I$ . Only a slight complication is that  $\mathcal{F}|_I$  is a map  $(X_0, U_0) \mapsto (X_1, U_1)$ , while (14) gives  $\mathcal{M} : (\vartheta_0, \psi_0) \rightarrow (\vartheta_1, \psi_1)$ . Thus we have to convert  $\mathcal{M}$  to  $\mathcal{F}|_I$  as in (16) going back and forth between the different parametrization of the same point on  $I$ . From (3) and (13) we obtain for finite  $\chi$

$$X = 2 \cos \psi \frac{\cos^2 \vartheta + e^{-2\chi}}{1 + e^{-2\chi}}, \quad U = \sqrt{\mu} \arctan(e^\chi \cos \vartheta).$$

With  $\chi \rightarrow \infty$ , we observe

$$X \rightarrow 2 \cos \psi \cos^2 \vartheta, \quad U \rightarrow \sqrt{\mu} \operatorname{sign}(\cos \vartheta) \left( \frac{\pi}{2} - \frac{1}{e^\chi |\cos \vartheta|} \right).$$

Therefore, except for the critical case  $\theta = \pi/2$ , we can use the following relation for the necessary conversion;

$$X = 2 \operatorname{sign}(\cos \psi) \cos^2 \vartheta, \quad U = \frac{\pi\sqrt{\mu}}{2} \operatorname{sign}(\cos \vartheta), \quad (\text{A.4})$$

where for  $X$  we have used the fact that, on the Poincaré section  $y = 0$ , either  $\psi = 0$  (the case  $X > 0$ ) or  $\psi = \pi$  (the case  $X < 0$ ). This is (17) in the text.

To extract  $\mathcal{F}_I$  from  $\mathcal{M}$ , it is best to follow [2]. Fix  $\psi_0 = 0$  (that is, choose  $X_0 > 0$ ), and let  $\vartheta_0$  increase from 0 to  $\pi$ . (This is sufficient thanks to the symmetry of the system.) This makes  $(X_0, U_0)$  circulates around the boundary of the half-Gutzwiller rectangle. (See figure 4). On the other hand, follow the stream line in figure A1 until it reaches the next PSS, that is, until it crosses either  $\psi_1 = 0$  or  $\psi_1 = \pi$ . In this way, one can read off the final  $(\vartheta_1, \psi_1)$  for  $\mathcal{M}$  and, via (A.4), one gets  $(X_1, U_1) \in I$  for  $\mathcal{F}_I$ .

Now let us study the flow in figure A1. It has two types of singularities for  $\gamma < (\pi/9)$

$$(b) \text{ Hyperbolic : } \cos \vartheta = \cos \phi = 0 \quad [(\vartheta, \phi) = (m + \frac{1}{2}, n + \frac{1}{2})\pi, \quad m, n \in \mathbb{Z}] \quad (\text{A.6})$$

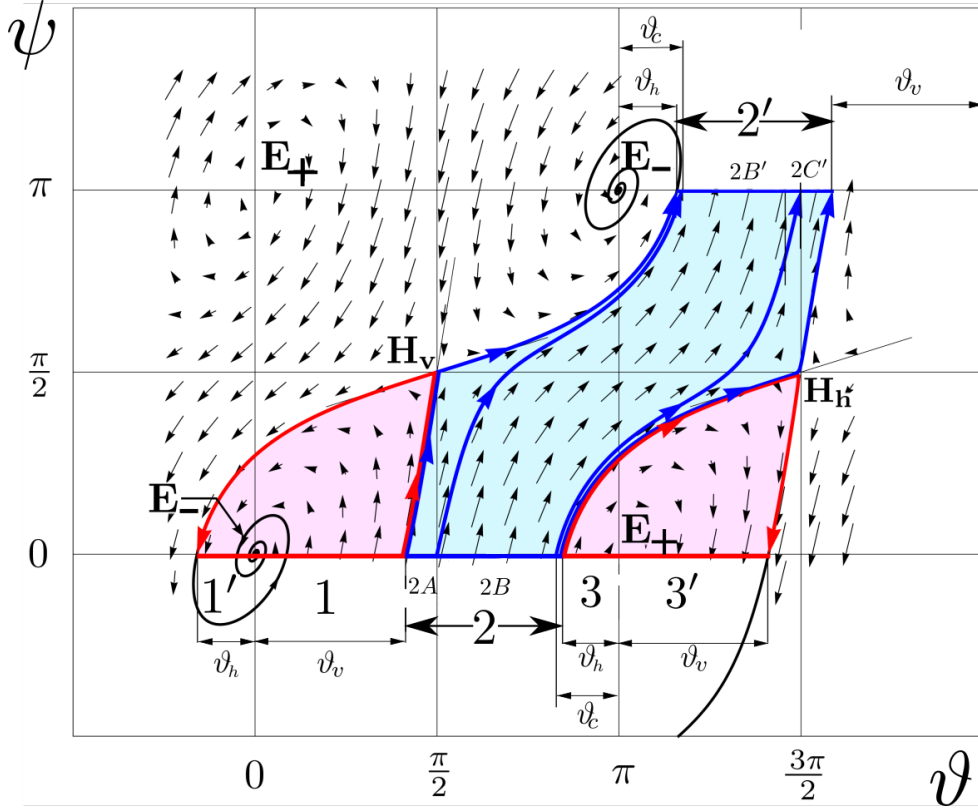


**Figure A1.** The flow given by the autonomous ODE (14 (The flow is the same with Fig. 1 in Gutzwiller [2] and equivalent to Fig. 2 in Devaney [16].) The anisotropy is  $\gamma = 0.2$ . The initial fundamental domain is divided into three regions 1, 2, 3 due to the hyperbolic singularities  $H_v$  and  $H_h$ . The region 2 is further divided into three sub-regions by the stream line with  $\vartheta_0 = \pi/2$  and that with  $\vartheta_1 = 3\pi/2$ . ( $2C$  and  $2A'$  are too narrow to indicate by letters.)

By the shift of  $\pi$  either in  $\vartheta$  or  $\psi$ , the linearized matrix and its eigenvalues change the sign. Therefore, a source ( $E_+$ ) and a sink ( $E_-$ ) locate alternatively at every  $\pi$  on the lattice (a). On the other hand, on the lattice (b), hyperbolic singularity  $H_v$  and  $H_h$  locate alternatively, where  $H_v$  ( $H_h$ ) attracts the trajectory vertically (horizontally).

The flow divides the initial domain into three regions, depending on whether the next crossing of the  $y$ -axis occurs with  $X_1 > 0$  ( $\psi_1 = 0$ ) or with  $X_1 < 0$  ( $\psi_1 = \pi$ ). The division is determined by two critical angles  $\vartheta_v$  and  $\vartheta_h$  [2]. The three regions are as follows.

- 1** :  $0 \leq \vartheta_0 < \vartheta_v$ ; the stream line is repelled by  $H_v$  to the left, and then attracted into  $E_-$  rotating counter-clockwise.  $0 \geq \vartheta_1 > -\vartheta_h$  and  $\psi_1 = 0$ .
- 2** :  $\vartheta_v < \vartheta_0 < \pi - \vartheta_h$ ; it is repelled by both  $H_v$  and  $H_h$ , and reaches  $\psi_1 = \pi$ . Thus,  $\pi + \vartheta_h < \vartheta_1 < 2\pi - \vartheta_v$  and  $\psi_1 = \pi$ .
- 3** :  $\pi - \vartheta_h < \vartheta_0 \leq \pi$ ; the repulsion by  $H_h$  acts to the right and the rotation by  $E_+$  is clockwise.  $\pi + \vartheta_v > \vartheta_1 \geq \pi$  and  $\psi_1 = 0$ .

For the map  $\mathcal{M}$  (the  $\vartheta\psi$ -representation), this division is sufficient. However, the

restricted map  $\mathcal{F}|_I$  (the  $XU$ -representation) uses the conversion via (A.4). This introduces further criticality at  $\vartheta_0 = \pi/2$  and  $\vartheta_1 = 3\pi/2$  and, as the consequence, region 2 is divided into three sub-regions for  $\mathcal{F}_I$ .

We should add that the most important for the above derivation of  $\mathcal{F}_I$  is the order of initial critical angles

$$\vartheta_v < \pi/2 < \pi - \vartheta_c < \pi - \vartheta_h. \quad (\text{A.7})$$

(The order of final critical angles  $\pi + \vartheta_h < \pi + \vartheta_c < \pi + \vartheta_h < 3\pi/2 < 2\pi - \vartheta_v$  is then guaranteed by the time-reversal symmetry). The order (A.7) follows from the distribution of the singularities in (A.6) for  $\gamma < 8/9$ , and the numerical confirmation is shown in figure A2.

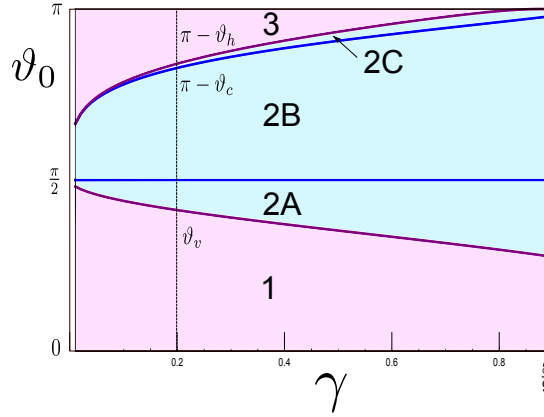


**Figure A2.** The variation of critical angles separating the fundamental domain  $\vartheta_0 \in [0, \pi], \phi = 0$  into 1, 2A, 2B, 2C, 3 for the anisotropy region  $\gamma < 8/9$ . At the canonical high anisotropy  $\gamma = 0.2$  corresponding to figure A1,  $\vartheta_h = 0.319039058$ ,  $\vartheta_c = 0.344255689$ ,  $\vartheta_v = 0.823746449$  in unit of  $\pi/2$ .

## Appendix B. One-time Map: Blow-up and Contraction

We use below symbols for critical objects to help the book-keeping. All in the domain of  $\mathcal{F}$  have naturally superscript ‘0’, and those in the image ‘1’. The side of a separator curve  $C$  has double subscript common to its adjacent region. A focus point is expressed by a letter ( $v, h$  and  $c$ ), taken from the subscript of the critical angle ( $\vartheta_v, \vartheta_h$  and  $\vartheta_c$ ), by which the  $X$ -coordinate of the point is determined. For instance,  $C_{++}^0$  is the side of a separator in  $D_0$  and adjacent to  $(++)$ , and  $v_{++}^1$  is a focus point in  $D_1$ , adjacent to  $(++)'$ , and  $X_v = 2 \cos^2 \vartheta_v$ . See table 1.

Let us start by examining how  $C_{++}^0$  is mapped by  $\mathcal{F}$ , since  $\mathcal{F}$  on  $(++)$  is relatively simple without rotation. Figure B1 shows how sets of vertical and horizontal line segments (set b and c), meeting at the separator  $C_{++}^0$  are mapped by  $\mathcal{F}$ . We observe every set turns into a ‘beak’ with its tip at  $v_{++}^1$ , while the full vertical line (a) not touching  $C_{++}^0$  is simply distorted. Thus we find a rule of contraction

$$\mathcal{F} : C_{++}^0 \mapsto v_{++}^1. \quad (\text{B.1})$$

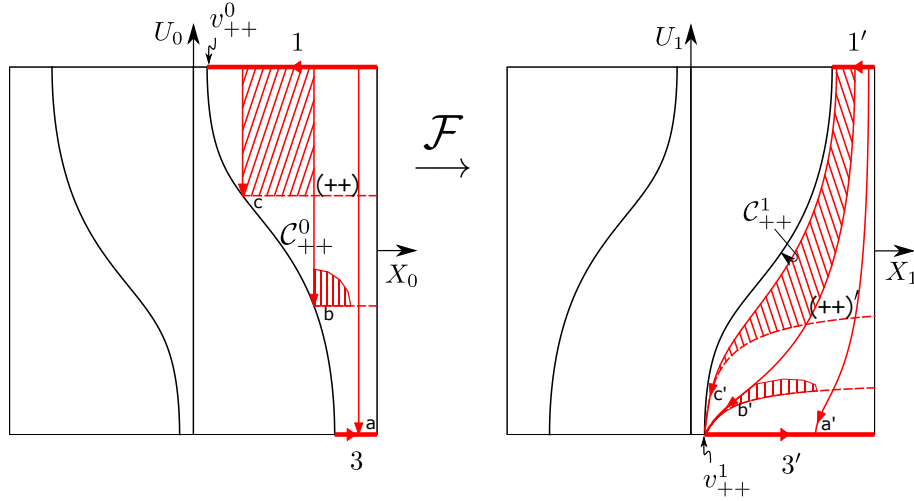


**Figure B1.** The action of  $\mathcal{F}$  on  $(+-)$ . Figure is to scale ( $\gamma = 0.2$ ). Hatched regions are mapped preserving area and orientation.  $C_{++}^0 \mapsto v_{++}^1$ .

By considering a move of vertical line segment (and its image in  $(++)'$ ) until it reaches  $v_{++}^0$ , we find a rule of blow up;

$$\mathcal{F} : v_{++}^0 \mapsto C_{++}^1. \quad (\text{B.2})$$

(B.1) and (B.2) are time-reversal pair. Now, let us proceed to the  $C_{(+-)}^0$ . It is adjacent to  $(+-)$  and  $\mathcal{F}|_I$  rotates the boundary 2 as seen in figure 4. We clarify in figure B2 how the rotation affects the interior map.

- (i)  $\mathcal{F}$  maps each set of vertical and horizontal line segments  $(p, q, \dots)$  meeting at  $C_{+-}^0$  into a *beak* with its tip at a point  $v_{+-}^1$ . Therefore,

$$\mathcal{F} : C_{+-}^0 \mapsto v_{+-}^1. \quad (\text{B.3})$$

This just corresponds to the contraction rule (B.1). On the other hand, the body of the beak reflects the rotation as follows.

- (ii) The left-side of the beak (dashed line) always connects the  $v_{+-}^1$  and another critical point  $c_+^1$ . And it is the image of the line segment horizontally connecting  $C_{+-}^0$  to  $\mathcal{I}_+^0$  (the  $X > 0$  side of the enter line of the collision manifold I in  $D_0$ ). Therefore, we find a contraction rule

$$\mathcal{F} : \mathcal{I}_+^0 \mapsto c_+^1. \quad (\text{B.4})$$

- (iii) The right-side of the beak, on the other hand, is the image of the vertical line segment connecting  $C_{+-}^0$  to either  $2B$  or  $2C$ . In the former, it is simply a long vertical curve. In the latter, it is a short *hook*, connecting  $v_{+-}^1$  and a point in  $2C'$ , now in the upper boundary due to the rotation.

Now, let us investigate the vertical line segments  $(a, b, c, \dots)$  connecting  $2A$  to  $2B$ .

- (iv) By the rotation,  $2A'$  and  $2B'$  are both in the bottom boundary of  $(+-)'$ . Thus,  $a', b', c', \dots$  form *wing*-like curves— folding, induced by the rotation. The limit



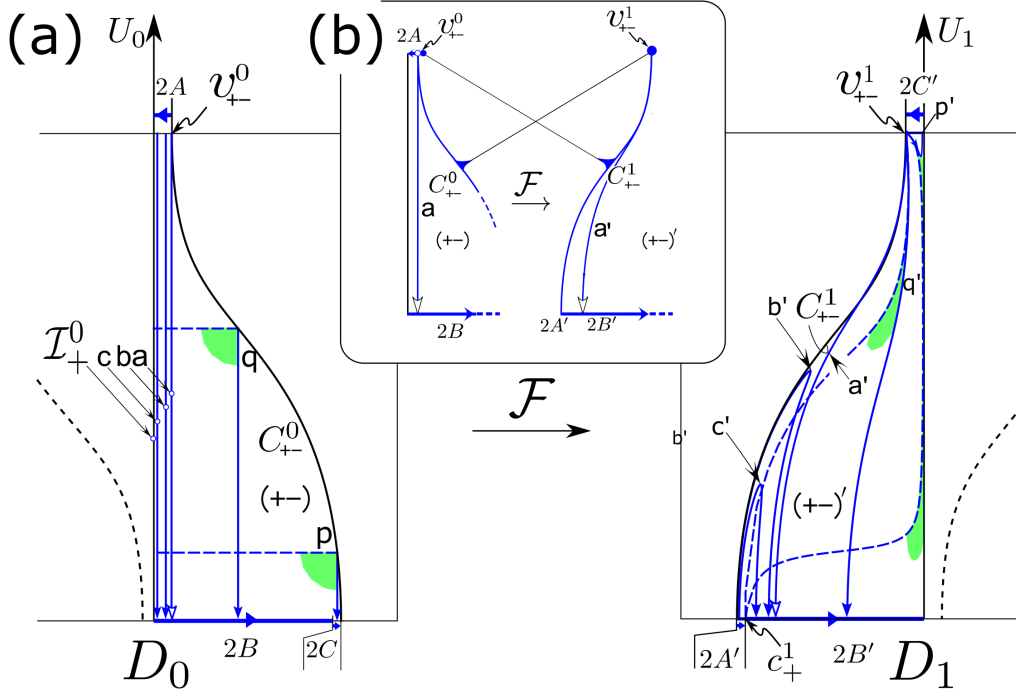


**Figure B2.**  $\mathcal{F}$  on  $(+-)$ . (a) The beaks ( $p'$  and  $q'$ ) show  $C_{+-}^0 \mapsto v_{+-}^1$ , while their bottoms reflect rotation (Compare a hook of  $p'$  with a vertical curve of  $q'$ ). Wings ( $b', c'$ ) contracts a focusing point  $c_+$ , showing  $\mathcal{I}_+ \mapsto c_+$ . (b) The vertical line segment  $a$  is critical. Body of  $a$  makes a curve  $a'$ , its top end  $v_{+-}^0$  makes  $C_{+-}^1$ , and they together make a beak (enveloping wings), whose top  $v_{+-}^1$  is then the image of the  $C_{+-}^0$ .

$a, b, c, \dots \rightarrow \mathcal{I}_+$  corresponds to  $a', b', c', \dots \rightarrow c_+^1$ . Comparing Limits of both code, we find again  $\mathcal{F} : \mathcal{I}_+^0 \mapsto c_+^1$ .

- (v) Reversing the previous code, let us consider  $\mathcal{I}_+, c, b, \dots \rightarrow a$ . The image is a code, starting from a single point  $c_+^1$ , passing through enlarging wings, and the limit is a cusped curve enveloping all wings. See figure B2(b). Here occurs a blow up of the end-point of  $a$ , namely

$$v_{+-}^0 \mapsto C_{+-}^1. \quad (\text{B.5})$$

Remarkably, we observe in figure B2(b) that the contraction and blow-up come in a pair, keeping the perimeter length of the boundary. (See more in (18)).

### Appendix C. Transverse Crossing of Future and Past Tiling

Let us first note a remarkable fact that  $D_0$  and  $D_1$  consist of altogether 8 sub-regions, but that there are actually only two distinct shapes. Half are congruent to  $(++)$  in AKP and the other half to  $(+-)$ . See figure C1. This comes from the invariance of AKP under time reversal and parity transformations. First, the time reversal changes the direction of momentum while keeping the coordinate values. Namely,

$$T : (X, U) \rightarrow (X, -U)$$

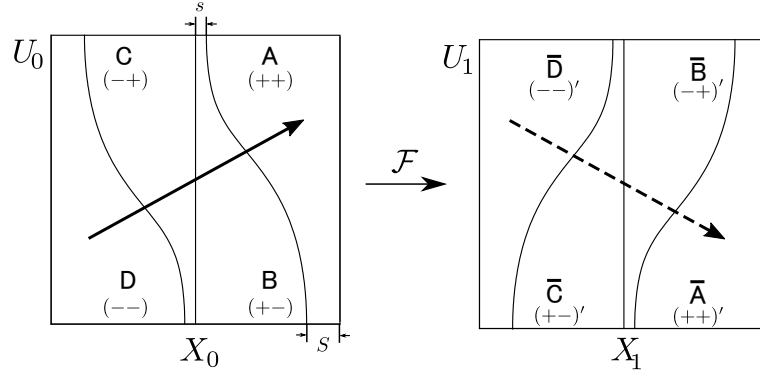


**Figure C1.** Four regions in  $D_0$ ;  $A(++), B(+--), C(-+), D(--)$  from right to left. Similarly  $\bar{A}(++)', \bar{B}(-+)', \bar{C}(+-)', \bar{D}(--)' \in D_1$  also from left to right. (Note the swap between  $(+-)$  and  $(-+)$  by  $\mathcal{F}$ ). There are only two distinct shapes;  $A$  with the shortest side  $S = 2 \cos^2 \vartheta_h$  and  $B$  with  $s = 2 \cos^2 \vartheta_v$  ( $S > s$ ). The direction of increasing DSS height is depicted by arrows, which are  $U \rightarrow -U$  mirror.

This in particular implies that an orbit with the initial value  $(X_0, U_0)$  and evolving backwards in time is the same with that starting with  $(X_0, -U_0)$  and evolves forward in time. Therefore, it follows for general  $N$  that

$$\zeta_P^N(X_0, U_0) = \zeta_F^N(X_0, -U_0) \quad (\text{C.1})$$

as a relation between the future and past height functions. Now, just as the sub-regions  $A, \dots, D$  are the ribbons of *future* height functions  $\zeta_{N=1}^F$ , so  $\bar{A}, \dots, \bar{D}$  are the ribbons of the past function  $\zeta_{N=1}^P$ , because  $(a_0, a_1) = (+-)$  for  $\mathcal{F}$  is equivalent to  $(a_0, a_1$  interchanged)  $(-+)'$  for  $\mathcal{F}^{-1}$  and so on. Therefore, it follows from time reversal symmetry that

$$\bar{A} \equiv A, \bar{B} \equiv B, \bar{C} \equiv C, \bar{D} \equiv D \pmod{U \rightarrow -U}. \quad (\text{C.2})$$

This is abbreviated below as  $\bar{A} \equiv T(A), \dots$ . Next, the symmetry under the parity transformation

$$\vec{x} \rightarrow -\vec{x}, \vec{p} \rightarrow -\vec{p}$$

implies that an orbit starting from  $(X_0, U_0)$  and its partner starting from  $(-X_0, -U_0)$  evolve keeping the relation  $X(t) = -\tilde{X}(t)$  (and hence  $a_n = -\bar{a}_n$ ). Therefore,

$$\zeta_N^F(X_0, U_0) = -\zeta_N^F(-X_0, -U_0), \quad \zeta_N^P(X_0, U_0) = -\zeta_N^P(-X_0, -U_0)$$

and we find that

$$A \equiv P(D), B \equiv P(C), \bar{A} \equiv P(\bar{D}), \bar{B} \equiv P(\bar{C}), \quad (\text{C.3})$$

where  $P$  acts on  $D_0$  as well as  $D_1$  as  $P: X \rightarrow -X, U \rightarrow -U$ . Finally, (C.2) and (C.3) together the eight sub-regions  $\bar{A}, \dots, \bar{D}$ , and  $\bar{A}, \dots, \bar{D}$  are grouped into two classes;

$$A \equiv T(\bar{A}) \equiv P(D) \equiv P(T(\bar{D})), \quad (\text{C.4})$$

$$B \equiv T(\bar{B}) \equiv P(C) \equiv P(T(\bar{C})). \quad (\text{C.5})$$

Now, the direction of increasing height of the future  $N = 1$  surface is shown by an arrow in figure C1. This is nothing but the  $N = 1$  fact in the proof of the properness of ribbon tiling by mathematical induction. Now, by the above symmetry relation, the arrow for the past  $N = 1$  surface is  $U \rightarrow -U$  mirror of the future arrow. Therefore, the future ribbons and past ribbons are transverse each other. This inherits to higher level ribbons, as the level  $N \rightarrow N + 1$  proceeds keeping the properness of ribbon tiling. The sole exception is where future and past ribbons become tangent each other as seen in section 3.

## Appendix D. Transverse Chopping and Longitudinal Splitting

If one is content with just comparing the location of the new and previous ribbons, it is simple; each of previous ribbon *longitudinally* splits into two finer ones and just that. The height  $\zeta_N^F(X_0, U_0)$  of level  $N$  step is calculated by (6) from  $a_j, j = 0, \dots, N$  and  $\zeta_{N+1}^F(X_0, U_0)$  has additional last bit  $a_{N+1}$  which contributes  $\pm\Delta_{N+1}$  ( $\Delta_{N+1} = 1/2^{N+1}$ ). Here the sign depends on  $(X_0, U_0)$  via  $\mathcal{F}^{N+1}$ . But, as we proved, the tiling at  $N + 1$  is proper. Therefore, the level  $N$  ribbon longitudinally splits into two finer ribbons in such a way that the left of split-line gets  $-\Delta_{N+1}$  and right gets  $\Delta_{N+1}$ . See figure D1. Note, in the case of non-shrinking ribbon, the longitudinal split-line occurs on the boundary of a level  $N$  ribbon. The level  $N + 1$  ribbons are created by chopping the  $N$  ribbons

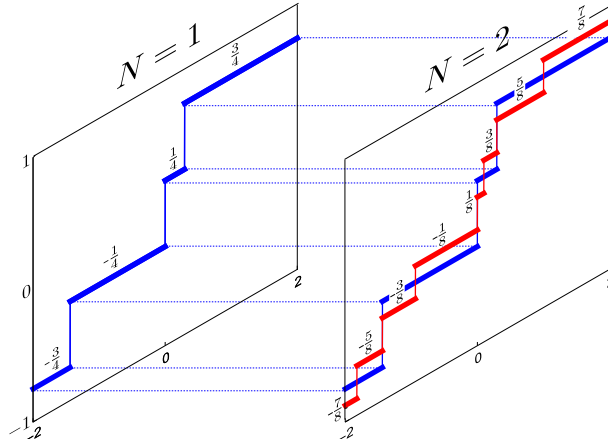


**Figure D1.**  $N = 1, 2$  DSS are compared by sections at  $U_0 = B/2$  ( $\gamma = 0.2$ ). (See also  $N = 2 \rightarrow 3$  tiling-evolution in figure 8). Next ribbons are created by *transverse* chopping+separation+elongation, but it looks as a simple *longitudinal* splitting of every ribbon, if one does not care which (half of) ribbon goes to which one of new ribbons.

*transversely* into two parts by the (fixed) separator curve and mapping each into different half of rectangle with elongation from  $-B$  to  $B$  as shown in section 3. So, if one picks some ribbon at large  $N$ , and wishes to trace back from which part of initial domain it comes, it requires tremendous task. See figure D2.

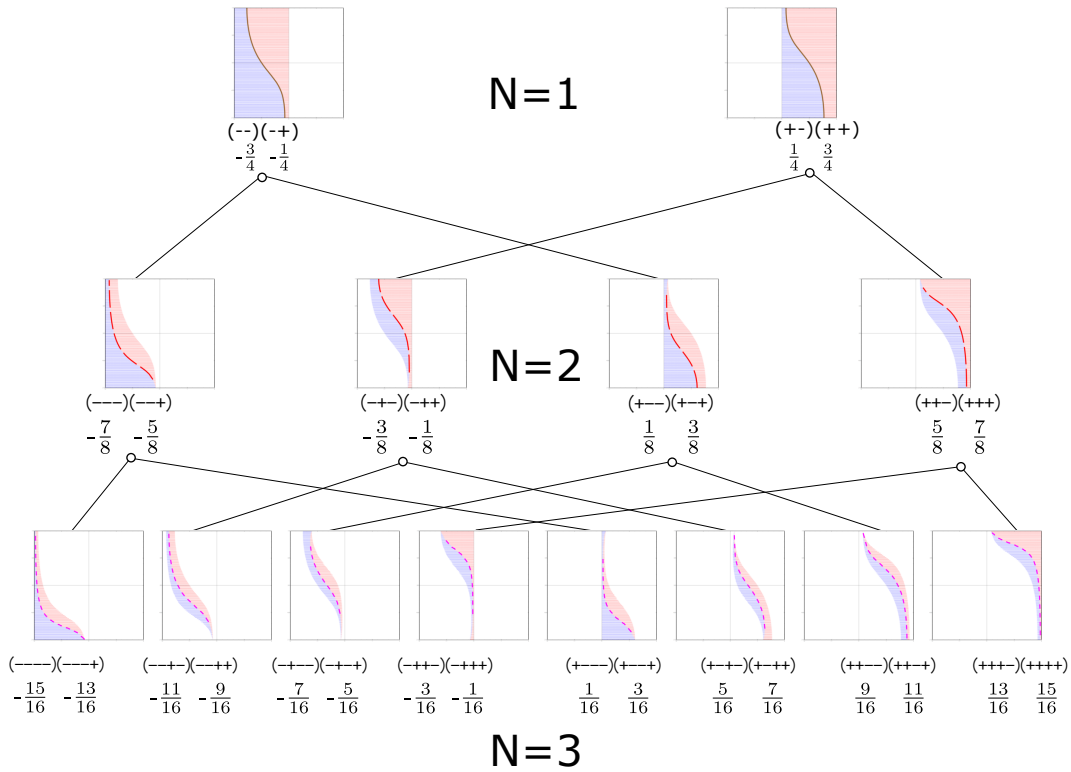


**Figure D2.** From the level  $N = 1$   $2^2$  ribbons, higher level ribbons ( $2^3$  at  $N = 2$ ,  $2^4$  at  $N = 3$ ) are created by repeated application of  $\mathcal{F}^{-1}$  and lines to track descendants are shown. It is extremely hard to track-back to the parent already through  $\mathcal{F}^{-2}$  (twice the baker-map).

### Appendix E. Uniqueness of PO within the Overlap

As for the unstable PO3-6, the initial position is remarkably very close to the edge of the overlap. This is just as it should; the unstable PO must be, to be a PO, on the union of future and past ribbons of its code, and yet, to be unstable, *should not be* much inside the junction. This is a subtle point, since the exact corner is homo-clinic point and cannot be a periodic point. The fact is that the unstable PO3-6 turns out extremely close to the corner as shown in figure E1. We thank Tanikawa and Shibayama pointing out this issue of homo-criticality and mentioning that this kind of close proximity often occurs. The unstable PO3-6 is non-self-retracing ('NR'). There is no other PO of the same code on the union of the future and past ribbons as is also clear in figure E1. We should add that we have observed stable satellite in the Broucke's island. The detail is under investigation.

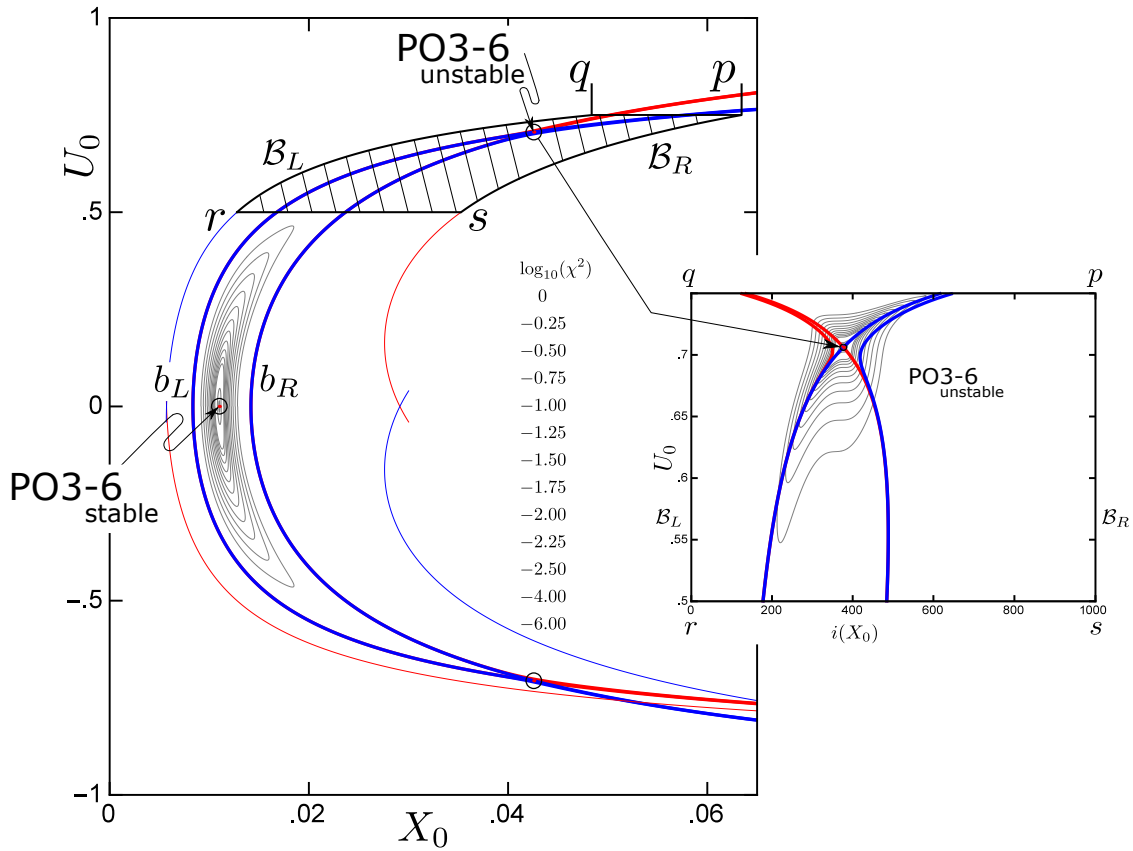


**Figure E1.**  $\chi^2$  contours showing that no period 6 PO other than PO3-6 (rank 3 id 6)  $S$  and  $U'$  (figure ??) exists inside Broucke's non-shrinking ribbon.  $\gamma = 0.6$ . Union of future and past ribbons has asymptotic boundaries  $b_L$  and  $b_R$  ( $N = 48$ ), which is well inside the  $N = 6$  union ( $\mathcal{B}_L$  to  $\mathcal{B}_R$ ). Inside the latter, a fine mesh of initial points ( $10^3 \times 10^3$ ) is set and  $\chi^2$  ((34),  $2n = 6$ ) is calculated for each point. This is a fail-safe procedure as well as a useful device for magnifying near the narrow edge region. The equi-contours focus the  $S$ . Inset: The same  $\chi^2$  contours in  $pqr$ s (after a stretch in the  $X$  direction). They focus the unstable  $U'$  at the edge.

## References

- [1] M. C. Gutzwiller, J. Math. Phys. **12**, pp.343-358 (1971).
- [2] M. C. Gutzwiller, J. Math. Phys. **18**, 806 (1977).
- [3] M. C. Gutzwiller, Phys. Rev. Lett. **45**, pp.150-153, (1980).
- [4] M. C. Gutzwiller, Periodic orbits in the anisotropic Kepler problem, pp. 69-90 in *Classical Mechanics and Dynamical systems*, Devaney, R. L. & Nitecki, Z. H. (ed.), Lecture note in pure and applied mathematics **70**, Marcel Dekker, New York, (1981).
- [5] M. C. Gutzwiller, J. Phys. Chem. **92**, pp. 3154-3163 (1988).
- [6] M. C. Gutzwiller, Physica **D38**, pp.160-171 (1989).
- [7] M. C. Gutzwiller, *Chaos in Classical and Quantum Mechanics*, Springer (1990).
- [8] D. Wintgen and H. Marxer, Phys. Rev. Lett. **60**, pp. 971-974, (1988).
- [9] A. M. García-García and J. J. M. Verbaarschot, Phys. Rev. **E 67**: 046104-1 - 046104-13.
- [10] A. M. García-García and J. Wang, Phys. Rev. Lett. **100**: 070603-1 - 070603-4.
- [11] K. Kubo and T. Shimada, Anisotropic Kepler Problem and Critical Level Statistics, in *Theoretical Concepts of Quantum Mechanics*, InTech (Open Book), 2012.

- [12] K. Kubo and T. Shimada, Prog. Theor. Exp. Phys., 023A06 (2014).
- [13] K. Sumiya, H. Huchiyama, K. Kubo and T. Shimada, Classical and Quantum Correspondence in Anisotropic Kepler Problem, in *Advances in Quantum Mechanics*, InTech (Open Book), 2013.
- [14] Z. Chen *et al.*, Phys. Rev. Lett. **102**, 244103, pp.1-4 (2009).
- [15] W. Zhou *et al.*, Phys. Rev. Lett. **105**, 024101, pp.1-4 (2010).
- [16] R. L. Devaney, Inventiones. Math. **45**, 221-251 (1978).
- [17] R. M. McGehee, Inventiones. Math. **27**, 191-227 (1974).
- [18] R. Broucke, Collision orbits in the anisotropic Kepler problem, in *1985 Dynamical Astronomy*, ed. V G Szebehely and B Balazs (Austin, TX: Univiversity of Texas Press) p 9.
- [19] M. C. Gutzwiller [7], Section 11.3 and 20.7. The line, concerning Devaney's suggestion in the footnote is a quotation from the latter.
- [20] G. Contopoulos and M. Harsoula, J. Phys. A: Math. Gen. **38**, pp. 88978920 (2005).
- [21] K. Sumiya, K. Kubo and T. Shimada, Artif Life Robotics **19**, pp.262-269 (2014).
- [22] M. Kac, Phys. Fluid **2**, pp.8-12 (1959).
- [23] A. M. Ozorio de Almeida and J. H. Hannay, J. Phys. A: Math. Gen. **20**, pp.5873-5883 (1987).
- [24] J. Main, Phys. Rep. **316**pp. 233-338 (1999).
- [25] H. Schomerus and F. Haake, Phys. Rev. Lett. **79**, pp.1022-1025 (1977)